Prediction and optimization of condensation heat transfer coefficients and pressure drops of R134a inside an inclined smooth tube

S. M. A. Noori Rahim Abadi, M. Mehrabi*, J. P. Meyer

Department of Mechanical and Aeronautical Engineering, University of Pretoria, Pretoria, Private Box X20, Hatfield 0028, South Africa

*Corresponding author. Tel.: +27 12 420 4743

E-mail address: mehdi.mehrabi@up.ac.za

Abstract:

In this study, an adaptive neuro-fuzzy inference system (ANFIS) is proposed for the prediction and optimization of condensation heat transfer coefficient and pressure drops along an inclined smooth tube. The performance of three ANFIS structure identification methods, grid partitioning (GP), a subtractive clustering method (SCM), and fuzzy C-means (FCM) clustering, were examined. For training the proposed ANFIS model, an in-house experimental database was utilised. Three statistical criteria, the mean absolute error (MAE), mean relative error and root mean square error were used to evaluate the accuracy of each method. The results indicate that the GP structure identification method has the lowest number of training errors for both the pressure drop, *i.e.*, MAE = 6.4%, and condensation heat transfer coefficient, *i.e.*, MAE = 2.3%, models. In addition to the ANFIS model, numerical simulations were also conducted to assess the accuracy and capability of the proposed model. The comparison shows that the CFD simulation results have better accuracy for the specified operating conditions. However, the errors of both the CFD and ANFIS methods were within the uncertainties of the experimental data. It was therefore concluded that the ANFIS model is useful in obtaining faster and reliable results. Finally, the optimization results showed a possible optimum point at a mass flux of 100 kg/m^{2}s, saturation temperature of 36.2 °C, downward inclination angle of -15° and a vapour quality of 0.48. At this condition the pressure drop is almost zero.

Keywords: Condensation; ANFIS; CFD; Multi-objective optimization

Nomenclature

A	Membership function in ANFIS structure [-]
$a_{i,j}$	Consequent parameter matrix
B	Membership function ANFIS structure [-]
$b_{i,j}$	Consequent parameter matrix
E	Internal energy [J]
f	Firing strength in ANFIS structure [-]
F	Source term in the momentum equation [N/m^3]
g	Gravitational acceleration [m/s^2]
G	Mass flux [kg/m^{2}s]

G_b	Generation of turbulence kinetic energy due to buoyancy, [m^4/s]
h	Heat transfer coefficient [W/m^2K]
k	Turbulent kinetic energy [m^2/s^2]
M	Node label in layer 2 in ANFIS structure [-]
N	Node label in layer 3 in ANFIS structure [-]
P	Pressure [Pa]
q''	Heat flux [W/m^2]
S	Summation of all signals in ANFIS structure [-]
S_E	Energy source term [J/m^3s]
S_l	Condensation mass source term [kg/m^3s]
S_v	Vaporization mass source term [kg/m^3s]
t	Time [s]
T	Temperature [K]
T_{sat}	Saturation temperature [K]
u	Velocity [m/s]
$\bar{w}$	Normalized firing strength in ANFIS structure [-]
x	Input parameter in ANFIS structure [-]
X_a	Predicted value [-]
X_p	Actual (experimental) data [-]
y	Input parameter in ANFIS structure [-]

Greek symbols

α	Volume fraction [-]
μ	Molecular viscosity [Pa.s]
ρ	Density [kg/m^3]
k	Curvatures of liquid and vapour phase [-]
ε	Turbulent dissipation rate [m^2/s^3]
x	Vapour mass fraction [-]
β	Inclination angle [°]
σ	Surface tension [N/m]

Subscripts

ave	Average
eff	Effective
l	Liquid

L	Laminar
m	Mean
v	Vapour

Abbreviations

ANFIS	Adaptive Neuro-Fuzzy Inference System
FCM	Fuzzy C-means clustering
GP	Grid partitioning
MAE	Mean absolute error
MF	Membership function
MRE	Mean relative error
RMSE	Root mean squared error
SCM	Subtractive clustering method

1. Introduction

The applications of soft computing methods in the modelling and analysis of engineering problems have increased significantly during the last decade. Fuzzy logic, neural networks, and genetic algorithms are among the most frequently used components of soft computing methods. Because soft computing methods can recognise the existing knowledge and patterns behind empirical data, they have received significant attention within a wide range of mechanical engineering applications during the last few years [1-4].

Using experimental data, Gill and Singh [5] suggested the application of prediction models based on a dimensional analysis and the Adaptive Neuro-Fuzzy Inference System (ANFIS) method for an R134a/LPG mass flow in an adiabatic tube. Their results indicated that although both the dimensional analysis and ANFIS method, achieve good statistical performance, the accuracy of the ANFIS model is slightly better.

For better monitoring of wind turbine farms, Morshedizadeh *et al.* [6] introduced a new methodology based on a combination of an adaptive neuro-fuzzy inference system (ANFIS), an imputation algorithm, and a feature selection method to predict the performance of commercial wind turbines. To show the predictive capability of the suggested methodology, power curves of 2.3 MW pitch-regulated wind turbines were

investigated. The results indicate that the proposed ANFIS model performs better than the existing models.

Using an experimental dataset, ANFIS, and an artificial neural network (ANN), Seijo *et al.* [7] suggested the application of prediction models for 12 different systems within an actual combined heat and power (CHP) power plant. Their results indicated the capability of both approaches to model cogeneration power plant systems with high accuracy. After modelling, a multi-objective optimisation technique was applied to maximise the electric production and amount of heat used in the slurry process, and to minimise the fuel consumption.

An ANFIS and an ANN were utilised by Şahin [8] to predict the coefficient of performance (COP) of a single-stage vapour compression refrigeration system. Three environmental friendly refrigerants, R134a, R404a, and R407c, were used in this system. The same datasets were used for both ANFIS and ANN modelling. The results show that the ANN model performs better than ANFIS for R134a, whereas the prediction performance of the ANFIS is better than that of the ANN for R404a and R407c.

The applicability of an ANN for the identification of a two-phase flow regime has been investigated by various researchers [9, 10]. Pan *et al.* [10] developed a fuzzy C-means (FCM) clustering algorithm to create a flow regime identification map for a co-current air-water two-phase flow in the vertical direction. They conducted several experiments to build a suitable database. Their results indicate that the proposed fuzzy method can be applied to the successful identification of the flow regime for both upward and downward flows.

Balcilar *et al.* [11] used multilayer perceptron (MLP), radial basis networks (RBFN), and generalized regression neural network (GRNN) ANN methods, as well as the adaptive neuro-fuzzy inference system (ANFIS) technique for the prediction of the condensation heat transfer coefficient and pressure drop inside a vertical tube with a diameter of 8.1 mm. They used different refrigerant mass fluxes, saturation temperatures, and wall heat fluxes for training purposes. They examined the performances of above mentioned ANN

methods and ANFIS technique in their study. Their results indicate that the ANFIS, radial basis network (RBFN), and multi-layer perceptron (MLP) methods can predict the condensation heat transfer coefficient and pressure with a deviation of less than 20% as compared with the experiment data.

In addition to the development of the ANFIS model, numerical simulations of condensation inside an inclined smooth tube have been conducted. The purpose of the CFD simulation was to conduct an assessment of the accuracy and computational costs of the proposed ANFIS model. Literature reviews have shown that previous numerical studies on the condensation inside different tubes have been limited to horizontal or vertical orientations [12-15]. Numerical simulations have been recently conducted to investigate the effects of the inclination angle on the condensation heat transfer coefficient, pressure drop, and flow regimes inside a smooth tube. The results showed an optimum downward inclination angle of between -30° and -15° through which the heat transfer coefficients become maximum. It was also found that the effect of the inclination angle on the pressure drop and void fraction become negligible at a high mass flux and vapour quality [16].

Beside the applications of numerical methods for simulation and predicating purposes, their performance and ability to conduct optimization studies have been proven in the past. Genetic algorithm (GA) is one of the most favorite ones among evolutionary algorithms (EA) due to its simplicity and population-based search methodology. Applying different approaches for fitness assignment, elitism or diversification resulted in various genetic algorithm-based multi-objective optimization methods in literature [17].

In 2002 Deb *et al.* [18], proposed a modified non-dominated sorting genetic algorithm, called NSGA-II. This method later received significant attention as one of the most efficient genetic algorithm-based multi-objective optimization methods. Detailed information about this method has been given in Section 4. During the last fifteen years, NSGA-II was used in a wide range of mechanical engineering applications to find optimum design Pareto fronts [19-23].

Literature reviews have shown that there have been no studies investigating the potential of a neuro-fuzzy inference system to predict the inclination effect on condensation of a refrigerant in a smooth tube. Furthermore, no work has been done on the optimization of heat transfer coefficients and pressure drops during the condensation phenomenon inside an inclined smooth tube. It was therefore the purpose of this paper, to apply ANFIS-GP and to model and predict the condensation heat transfer coefficients and pressure drops along an inclined smooth tube. Furthermore, to use NSGA-II multi-objective optimization approach to find the Pareto front of condensation heat transfer and pressure drop. Also, a comparison was made of the time and computational costs between the CFD and ANFIS models.

2. Adaptive Neuro-fuzzy Inference System

An ANFIS is built based on a combination of an ANN and fuzzy logic techniques. This combination creates a robust modelling for many different engineering problems. In an ANFIS, an ANN is used to find the appropriate membership functions and reduce the rate of errors in the rule determination process. On the other hand, a rule-based fuzzy inference system (FIS) in an ANFIS system transfers qualitative knowledge into an accurate quantitative analysis.

The ANFIS structure consists of two parts, *i.e.*, an introductory part and a conclusion part. A set of fuzzy rules links these two parts of the ANFIS structure together. Five district layers of a multilayer ANFIS network are shown in Fig. 1.

The first layer of the ANFIS structure combines all input and output data into a single input-output space, and applies the fuzzification later. The firing-strength of a rule is calculated in the second layer, which is called the "rule layer." This layer connects each node of the second layer with a fuzzy rule. The third layer conducts a normalisation of the membership functions by calculating the rate of the firing-strength associated with each rule for a summation of all rule firing-strengths. Defuzzification occurs in the fourth layer, which is the conclusive part of the fuzzy rules. Consequent parameters of the fuzzy rules are calculated in this layer. Finally, the last layer calculates the network outputs. Detailed information regarding the ANFIS structure layers was provided by Mehrabi *et al.* [24] and Rezazadeh *et al.* [25].

Grid partitioning (GP), a subtractive clustering method (SCM), and fuzzy C-means clustering (FCM) are three structure identification methods commonly used in an ANFIS system. The selection of input variables, input space partitioning, choice of the membership functions, creation of the fuzzy rules, and selection of the initial parameters for membership functions all take place during the structure identification process used by Jalalifar *et al.* [26].

GP, which is an ANFIS structure identification method, was initially introduced by Jang [27]. Using GP, a partition is formed by dividing the input space into several fuzzy rectangular subspaces using an axis-paralleled partition, each of which is specified by the fuzzy membership function and type for each feature dimension.

With this method, fuzzy grids are used to generate fuzzy rules based on the input-output dataset. The GP performance depends heavily on the definition of the grid. The gridding process can be refined with the use of an adaptive approach. In this approach a uniform partitioned grid is utilized for the initialisation at the first step, then the previous membership functions are adjusted, and therefore the fuzzy grid evolves. At the next step the size and location of the fuzzy grid is optimized by using gradient descent method. Because the number of fuzzy rules increases exponentially with the increase in the number of input variables, Jang [27] suggested that a grid partitioning method is only suitable for cases with less than six input variables.

The SCM as a fuzzy clustering technique was first introduced by Chiu [28] in 1994. With this algorithm, each data point is considered a potential cluster centre. The probability of this potential for each data point is calculated based on the density of the surrounding data points. After calculating this potential for each data point, the one with the highest probability is chosen as the first cluster centre. The potential of all data points near the first cluster centre being another cluster centre is reduced, and these data points are not considered in the next cluster centre selection process. This iterative process of selecting cluster centres and reducing the potential of neighbouring data points continues until all data points are within the range of influence of a cluster centre.

The FCM clustering algorithm was initially introduced by Dunn [29] and later Bezdek [30] and Bezdek *et al.* [31] as a data clustering technique in which each data point belongs to two or more clusters. The purpose of this unsupervised iterative algorithm is to find cluster centres based on a minimisation of the sum of the weighted square distances between each data point and the cluster centres. With the FCM algorithm, the number of clusters and the fuzziness index are first selected at random. The algorithm then begins by initialising the cluster centres using a random value from the data points. The next step, the membership matrix is computed and after the computation of the membership matrix, the objective function is computed. Finally, the new fuzzy cluster centres are computed. This iterative process is continued until the objective function is lower than the termination criteria.

3. Multi-objective optimization

In many engineering applications, we are dealing with different objectives that most of the times are competing. The best example of that in thermal science problems is where attempts are normally made to increase the heat transfer rate which unfortunately results in higher pressure drop and thus pumping power, which is undesirable. Multi-objective optimization techniques are the answer to those engineering problems that involve more than one objective function or conflicting objective functions.

There is not always a unique solution that optimizes all the parameters simultaneously. However, there may exist a set of Pareto optimal solutions. A solution is called non-dominated or Pareto optimal if none of the objective functions can be improved in value without degrading one or more of the other objective values. Various multi-objective algorithms have been applied in engineering in the last two decades. Since the NSGA-II algorithm (Non-dominated sorting genetic algorithm II) is one of the most effective ones among them, it was chosen for this paper.

The NSGA-II algorithm, has different operators that should work together to create a robust multi-objective optimization technique. Information on the operators such as; the fast non-dominated sorting operator, crowding-distance-assignment operator, and simulated binary crossover (SBX) operator. How they are connected to each other, and a flow diagram of the algorithm have been given in the previous work of the second

author [21]. The condensation heat transfer coefficient and pressure drop were two competing objectives in this study. The goal of the optimization process in this paper was to find the best design variables to maximize the condensation heat transfer coefficient and minimize the pressure drop simultaneously with respect to the mass flux G, saturation temperature T_{sat}, vapor quality x, and inclination angle β, which were the design variables.

4. CFD simulation

In this study, numerical simulations were also conducted to assess the performance of the proposed ANFIS model. To do so, a volume of fluid (VOF) multiphase flow formulation [32] is used for a simulation of the condensation phenomenon inside an inclined tube. In the VOF model, the governing equations, i.e., continuity, momentum, and energy equations, are defined as follows [16]:

$$\frac{\partial \alpha_v}{\partial t} + \nabla.(\vec{u}\alpha_v) = \frac{S_v}{\rho_v} \tag{1}$$

$$\alpha_l = 1 - \alpha_v \tag{2}$$

$$\frac{\partial(\rho_m \vec{u})}{\partial t} + \nabla.(\rho_m \vec{u}\vec{u}) = -\nabla p + \nabla.[\mu_{m,eff}(\nabla\vec{u} + (\nabla\vec{u})^T)] + \rho_m \vec{g} + \vec{F}_\sigma \tag{3}$$

$$\frac{\partial(\rho_m E)}{\partial t} + \nabla.[\vec{u}(\rho_m E + p)] = \nabla.(k_{m,eff}\nabla T) + S_E \tag{4}$$

where α is the volume fraction; u is the velocity; t is time; parameter S is the source term owing to a phase change; and indices l, v, and are the liquid, vapour, and mixture phases, respectively. Moreover μ_{eff}, k_{eff}, ρ, p, g, E, and F_σ are the effective viscosity, effective thermal conductivity, density, pressure, gravitational acceleration, internal energy, and surface tension force, respectively.

For modelling the turbulence, a two-equation turbulence model, k-ε, is applied. The equations of turbulence energy and dissipation rate are as follows [33]:

$$\frac{\partial(\rho_m k)}{\partial t}+\nabla.(\rho_m \vec{u} k)=\nabla.[(\mu_{L,m}+\frac{\mu_{t,m}}{\sigma_k})\nabla k]+[\mu_{t,m}(\nabla\vec{u}+(\nabla\vec{u})^T):\nabla.\vec{u}]-\rho_m\varepsilon+G_b \quad (5)$$

$$\frac{\partial(\rho_m \varepsilon)}{\partial t}+\nabla.(\rho_m \vec{u} \varepsilon)=\nabla.[(\mu_{L,m}+\frac{\mu_{t,m}}{\sigma_\varepsilon})\nabla\varepsilon] + \frac{\varepsilon}{k}(C_{1\varepsilon}[\mu_{t,m}(\nabla\vec{u}+(\nabla\vec{u})^T):\nabla.\vec{u}]-C_{2\varepsilon}\rho_m\varepsilon)+C_{1\varepsilon}C_{3\varepsilon}\frac{\varepsilon}{k}G_b \quad (6)$$

where k and ε are the turbulent kinetic energy and turbulent energy dissipation rate, respectively. The parameter G_b is the generation of turbulence kinetic energy due to buoyancy. Further details on the constants used can be found in [33].

In this study, the effect of the phase is considered using the source terms in the governing equations. The condensation source terms can be expressed as in [34, 35]:

$$S_l = r_l \alpha_l \rho_l \frac{T-T_{sat}}{T_{sat}} \quad T \geq T_{sat} \quad (7)$$

$$S_v = r_v \alpha_v \rho_v \frac{T_{sat}-T}{T_{sat}} \quad T < T_{sat} \quad (8)$$

where T and T_{sat} are the temperature and saturation temperature of the working fluid, respectively. The coefficients r_l and r_v should be tuned to fit the model to the experiment data. Excessively small values of the coefficient r lead to a significant deviation between the interfacial and saturation temperatures. However, overly large values of r cause numerical convergence problems. In the present study, the values of r_l and r_v are both considered to be 5 500 s^{-1}.

The following assumptions are considered for the simulations:

1. The flow regimes are slug or annular. Therefore, it is always possible to capture a certain two-phase interface.
2. The flow field is considered to be three-dimensional, unsteady, and turbulent.
3. The velocity difference between the liquid and vapour phases is neglected.
4. The properties of each phase are assumed to be constant under the specified operating conditions.

5. The interface temperature is assumed to be equal to the saturation temperature.
6. The contact angle between a liquid and solid at a saturation temperature of 40 °C is set to 5.8° [36].
7. A constant heat flux of 250 W and a no slip condition are assumed at the tube wall.
8. As the initial condition, the whole volume of the tube is considered to be vapour with a constant temperature equal to the saturation temperature.

To solve the governing equations, the ANSYS FLUENT 17.1 commercial software package is utilised. The pressure-velocity coupling is achieved using a two-phase extension of the well-known SIMPLE algorithm. To attain a stable solution procedure, all convective fluxes are approximated using a second-order upwind method, whereas the diffusive fluxes are discretised through a central differencing. To capture the liquid/vapour interphase, the Geo-Reconstruction scheme is also utilised. Moreover, the convergence criterion is set to 10^{-5} for the residual of each parameter. A time-step size of 10^{-4} s is used for the simulations. Further details on the numerical simulation can be found in [16, 37].

The effect of grid size on the condensation heat transfer coefficient (Fig. 2 (a)) and pressure drop (Fig. 2 (b)) for two different operating conditions is presented in Fig. 2. The test cases for the condensation heat transfer coefficient and pressure drop are G = 200 kg/m²s, T_{sat} = 50 °C, and x_m = 0.5, and G = 100 kg/m²s, T_{sat} = 30 °C, and x_m = 0.25. Three grid sizes, with 640 000, 960 000 and 1 680 000 quadrilateral cells, are studied. In general, the results for each grid size show adequate consistency with the experimental data of Meyer *et al.* [38] for the condensation heat transfer coefficient and Adelaja *et al.* [39] for the pressure drop; however, it is concluded that the results for grid sizes greater than 960 000 cells changed by less than 4%. Therefore, the grid with 960 000 cells is used for all the simulations in this study.

5. Experiment apparatus

In this study, the experimental database of Meyer *et al.* [40-44] is used for training the proposed ANFIS model. A schematic of the experiment setup developed by Meyer and *et al.* [40-44] during the last seven years is shown in Fig. 3. The setup consists of a vapour-

compression cycle with a nominal cooling capacity of 10 kW, which circulates refrigerant R134a through two high-pressure condensation lines: a test section line and a bypass line. The test section is constructed using a tube-in-tube counter flow heat exchanger configured with water flowing in the annulus and refrigerant flowing through the test section. Condensation therefore occurs in the inner tube. The diameter of the inner tube test section is 8.38 mm, and its length is 1 488 mm. The outlet of the tube under the flow regimes was captured using a video camera by looking through a sight glass tube of nearly the same internal diameter as the test section tube. The inclination angle of the test section could be changed within a vertical range of -90° downward to +90° upward, with 0° representing a horizontal angle. The heat transfer rates during condensation were determined by measuring the mass flow rate through the annulus, and the increase in temperature from the inlet to the outlet of the annulus. The heat transfer coefficients were determined from the heat flux in the annulus, and from measurements of the average wall temperature of the inlet and outlet temperatures of the refrigerant. The heat transfer coefficients are therefore the average heat transfer coefficients over the test section lengths. The uncertainties of these average heat transfer coefficients are ±10%. The vapour qualities at the inlets and outlets of the test section are determined based on the energy balance using water-cooled pre- and post-condensers. The heat transfer coefficients were determined for mass fluxes of 100 to 600 kg/m^{2}s at saturation temperatures of 30 to 50 °C at different qualities and inclination angles. During the experiments, the heat transfer rate of condensation was kept constant at 250 W by controlling the mass flow rates and water inlet temperature through the annulus using a thermal bath.

6. Results and discussion

6.1. Validation of the proposed ANFIS models

In this study, the above-mentioned structure identification methods were used to identify the premised membership functions for the ANFIS models for the pressure drop and condensation heat transfer coefficient of R134a within an inclined smooth tube. Figs. 4 and 5 show the training error for two specific cases, i.e., T_{sat} = 40 °C, G = 100 kg/m^{2}s, x_m = 0.25 and x_m = 0.75 for each structural identification method, and the experimental input-output datasets [38, 39] used for training purposes, respectively. The results show that GP structure identification shows the lowest training errors for

both the pressure drop and condensation heat transfer coefficient for the R134a models. Three statistical criteria, i.e., the MAE, MRE, and RMSE, listed in Table 1 are used to show the performance of grid partitioning, subtractive clustering, and fuzzy C-means clustering structure identification methods during the ANFIS training phase. The results are shown in Tables 2 and 3. From these results, it can be concluded that for both the pressure drop and condensation heat transfer coefficient of the R134a models within an inclined smooth tube, the GP structure identification method has the lowest training error, and was therefore chosen to continue with the ANFIS modelling procedure.

Furthermore, the performances of the two ANFIS models were examined for predictive purposes. Figs. 6 and 7 show sample results of the examinations for the prediction of the condensation heat transfer coefficient and pressure drop along the tube. As the figures indicate, the performance of the GP structure identification method is superior to the other model. The prediction results for the SCM were completely out of bound under the specified operating conditions for the condensation heat transfer coefficient, and therefore the results are not shown in Fig. 6. This was probably due to the fact that the specified operating conditions for the method are outside of the cluster.

A total of 679 input-output experimental data points obtained from the literature [38, 39] were used to predict the condensation heat transfer coefficient and pressure drop of R134a in an inclined smooth tube. The experimental data were divided into two sections, i.e., 588 data points for training and 91 data points for testing.

The optimum ANFIS structure and the membership functions were obtained through the GP structure identification technique, in which the input variables were fuzzified using generalised bell-shaped membership functions labelled MF1 and MF2 for the condensation heat transfer coefficient and pressure drop of R134a in an inclined smooth tube. The parameters of these membership functions are given in Table 4.

The fuzzy rule base of our proposed ANFIS models for the condensation heat transfer coefficient and pressure drop of R134a in an inclined smooth tube is given in Tables 5 and 6, respectively. The optimum consequent parameters obtained after the ANFIS

training process are given in the Appendix, in which $[a_{i,j}]$ is the consequent parameter matrix for the condensation heat transfer coefficient, and $[b_{i,j}]$ is the consequent parameter matrix for the pressure drop, of R134a in an inclined smooth tube.

Fig. 8 shows the results of the ANFIS (GP) training process for the condensation heat transfer coefficient for different mass fluxes, vapour qualities, saturation temperatures, and tube inclination angles of the refrigerant. The plot clearly shows the high capability of the proposed ANFIS (GP) model for the prediction of the input data for the condensation heat transfer coefficient. The predicted results are within the uncertainty of the experiment data. Moreover, the proposed model can predict well the optimum points at which the condensation heat transfer coefficient reaches the maximum.

Fig. 9 shows similar plots of input data prediction of the pressure drop along the tube. The results indicate that the predicted values are in good agreement with the experiment data. The results for the prediction of the input data, some of which are shown in Figs. 8 and 9, confirm that the proposed ANFIS (GP) model can predict well the characteristic parameters for the condensation process of R134a inside an inclined smooth tube.

6.2. Assessment of prediction capability of the proposed ANFIS model

After successfully training the proposed ANFIS (GP) model, the performance of the model for the prediction of in-bound and out-bound conditions was examined. Fig. 10 shows the predicted results for the pressure drop along the tube using the ANFIS (GP) model for the case of T_{sat} = 40 °C, G = 100 kg/m^{2}s, and x_m = 0.5. As Fig. 9 indicates, the predicted results are in good agreement with the experiment data, which proves the high predictive capacity of the proposed ANFIS (GP) model.

Figs. 11 and 12 show the predicted results for the condensation heat transfer coefficient using the ANFIS (GP) model for two cases of T_{sat} = 35 °C, G = 200 kg/m^{2}s, and x_m = 0.5 (Fig. 11), and T_{sat} = 45 °C, G = 200 kg/m^{2}s, and x_m = 0.5 (Fig. 12). In these figures, the flow regime is stratified or stratified-wavy [38, 39], and as a result, the condensation heat transfer coefficient experiences a maximum point at the region between β = -30°

and β = -15°. The plots clearly show that the proposed model can predict this maximum point well.

6.3. Performance assessment of CFD and the proposed ANFIS model

Fig. 13 compares the predicted results of the ANFIS (GP) model with the CFD simulation for the pressure drop along the tube for the case of T_{sat} = 40 °C, G = 400 kg/m^{2}s, and x_m = 0.5. The plots show that the CFD simulation obtained more accurate results than the proposed ANFIS mode. However, the performances of both methods are similar to each other, particularly for the negative inclination angles.

Figs. 14 and 15 show another comparison for two additional cases of T_{sat} = 40 °C, G = 300 kg/m^{2}s, and x_m = 0.25 (Fig. 14), and T_{sat} = 40 °C, G = 100 kg/m^{2}s, and x_m = 0.5 (Fig. 15). Although, the CFD simulation results are more accurate than that of the proposed ANFIS model, the deviations of the ANFIS results are within the uncertainties of the experiment data. Since, the experimental data has been used for tuning the parameters in the CFD simulation and training the ANFIS proposed models, the processing time of the CFD simulations and the ANFIS modelling technique on top of the accuracy comparisons should be taken into consideration regardless of the time required for experimentations. The required time for the CFD simulation in this study is significantly higher than that of the ANFIS modelling technique. Therefore it can be concluded that the ANFIS modelling technique will be more useful to obtain faster but still reliable results.

6.4. Optimum operating conditions

Fig. 16 shows the Pareto front of the condensation heat transfer coefficients and pressure drops along the tube. All the presented points are the optimum points that correspond to different operating conditions. The range of variations in the operating conditions for the optimization process is presented in Table 7. The plots can be categorized into four regions. In the first region there is a linear relationship between the condensation heat transfer coefficients and pressure drops. The values of the condensation heat transfer coefficients are low, varying from 1 000 to 1 900 W/m^{2}K with the pressure drops between -4 to -2 kPa in the first. Therefore the ultimate optimum operating conditions are not located in region one. In the second region, the

variations of the condensation heat transfer coefficients are linear with respect to the pressure drops, similar to the first region, but the values of the condensation heat transfer coefficients are much larger. In the third and fourth regions the slopes of variations of the condensation heat transfer coefficients with respect to the pressure drops are too high (as compared to the regions I and II). Although these two regions represent the optimum values for the specific operating conditions, these points cannot be considered as the ultimate optimum regions because of high values of the pressure drop along the tube.

The optimization process gave a unique optimum point in which the value of the pressure drop is almost zero compared, with a high condensation heat transfer coefficient of 2 647 W/m^{2}K. The corresponding operating conditions for this point are G = 100 kg/m^{2}s, T_{sat} = 36.1 °C, β = -15° and x_m = 0.48. Although the pressure drop for this point is not the minimum as compared to the points in region I, but the corresponding condensation heat transfer coefficient is about 40 % higher.

7. Conclusion

In the present work, an ANFIS was proposed for the prediction of the condensation heat transfer coefficient and pressure drop of R134a along an inclined smooth tube. Three different ANFIS methods were developed and their performances were studied. Moreover, CFD simulations were conducted for a suitable comparison between the timing and accuracy of the CFD and ANFIS models. Furthermore, the NSGA-II algorithm was used to find the optimum design points to reach the maximum condensation heat transfer coefficient and minimum pressure drop. Based on this study, the following conclusions can be made:

I. The results show that the ANFIS proposed models can predict well the characteristic parameters of condensation inside an inclined smooth tube.
II. The prediction results of the three ANFIS methods show that the GP method achieves better accuracy than the other two methods.
III. Although the CFD results show greater accuracy than the ANFIS model, the CFD method suffers from high computation costs.
IV. The ANFIS model will be more useful to obtain faster but still reliable results.

V. The multi-objective optimization showed a possible optimum heat transfer coefficient at a mass flux of 100 kg/m^{2}s, saturation temperature of 36.2°C, downward inclination angle of -15° and a vapour quality of 0.48 in which the pressure drop is almost zero and the condensation heat transfer coefficient is about 40 % higher compared to the points in region I.

References:

[1] S.A. Adio, M. Mehrabi, M. Sharifpur, J.P. Meyer, Experimental investigation and model development for effective viscosity of MgO-ethylene glycol nanofluids by using dimensional analysis, FCM-ANFIS and GA-PNN techniques, International Communications in Heat and Mass Transfer 72 (2016) 71-83.

[2] H. Benli, Determination of thermal performance calculation of two different types solar air collectors with the use of artificial neural networks, International Journal of Heat and Mass Transfer, 60 (2013) 1-7.

[3] S. Chanda, C. Balaji, S.P. Venkateshan, G.R. Yenni, Estimation of principal thermal conductivities of layered honeycomb composites using ANN-GA based inverse technique, International Journal of Thermal Sciences, 111 (2017) 423-436.

[4] L. Gosselin, M. Tye-Gingras, F. Mathieu-Potvin, Review of utilization of genetic algorithms in heat transfer problems, International Journal of Heat and Mass Transfer, 52 (2009) 2169-2188.

[5] J. Gill, J. Singh, Adaptive neuro-fuzzy inference system approach to predict the mass flow rate of R-134a/LPG refrigerant for straight and helical coiled adiabatic capillary tubes in the vapor compression refrigeration system, International Journal of Refrigeration, 78 (2017) 166-175.

[6] M. Morshedizadeh, M. Kordestani, R. Carriveau, D.S.K. Ting, M. Saif, Application of imputation techniques and Adaptive Neuro-Fuzzy Inference System to predict wind turbine power production, Energy, 138 (2017) 394-404.

[7] S. Seijo, I.d. Campo, J. Echanobe, J. García-Sedano, Modeling and multi-objective optimization of a complex CHP process, Applied Energy, 161 (2016) 309-319.

[8] A.Ş. Şahin, Performance analysis of single-stage refrigeration system with internal heat exchanger using neural network and neuro-fuzzy, Renewable Energy, 36 (2011) 2747-2752.

[9] E.S. Rosa, R.M. Salgado, T. Ohishi, N. Mastelari, Performance comparison of artificial neural networks and expert systems applied to flow pattern identification in vertical ascendant gas-liquid flows, International Journal of Multiphase Flow, 36 (2010) 738-754.

[10] L. Pan, M. Zhang, P. Ju, H. He, M. Ishii, Vertical co-current two-phase flow regime identification using fuzzy C-means clustering algorithm and ReliefF attribute weighting technique, International Journal of Heat and Mass Transfer, 95 (2016) 393-404.

[11] M. Balcilar, A.S. Dalkilic, S. Wongwises, Artificial neural network techniques for the determination of condensation heat transfer characteristics during downward annular flow of R134a inside a vertical smooth tube, International Communications in Heat and Mass Transfer, 38 (2011) 75-84.

[12] F. Behafarid, K.E. Jansen, M.Z. Podowski, A study on large bubble motion and liquid film in vertical pipes and inclined narrow channels, Interntational Journal Multiphase Flow, 75 (2015) 288-299.

[13] W. Fua, X. Li, X. Wu, M.L. Corradini, Numerical investigation of convective condensation with the presence of non-condensable gases in a vertical tube, Nuclear Engineering Design, 297 (2016) 197-207.

[14] J. Li, CFD simulation of water vapour condensation in the presence of non-condensable gas in vertical cylindrical condensers, International Journal of Heat Mass Transfer, 57 (2013) 708-721.

[15] C. Lin, D. Wang, A. Bao, Numerical modeling and simulation of condensation heat transfer of a flue gas in a bundle of transport membrane tubes, International Journal of Heat Mass Transfer, 60 (2013) 41-50.

[16] S.M.A.N.R. Abadi, J.P. Meyer, J. Dirker, Effect of inclination angle on the condensation of R134a inside inclined smooth tube, Chemical Engineering Research and Design, 132 (2018) 346-357.

[17] R.T. Marler, J.S. Arora, Survey of multi-objective optimization methods for engineering, Structural and Multidisciplinary Optimization, 26 (2004) 369-395.

[18] K. Deb, A. Pratap, S. Agarwal, T. Meyarivan, A fast and elitist multiobjective genetic algorithm: NSGA-II, IEEE Transactions on Evolutionary Computation, 6 (2002) 182-197.

[19] K. Foli, T. Okabe, M. Olhofer, Y. Jin, B. Sendhoff, Optimization of micro heat exchanger: CFD, analytical approach and multi-objective evolutionary algorithms, International journal of Heat Mass Transfer 49 (2006) 1090-1099.
[20] D. Copiello, G. Fabbri, Multi-objective genetic optimization of the heat transfer from longitudinal wavy fins, International Journal of Heat Mass Transfer, 52 (2009) 1167-1176.
[21] M. Mehrabi, M. Sharifpur, J.P. Meyer, Modelling and multi-objective optimisation of the convective heat transfer characteristics and pressure drop of low concentration TiO2-water nanofluids in the turbulent flow regime, International Journal of Heat and Mass Transfer, 67 (2013) 646-653.
[22] G.E.C. Caballero, L.S. Mendoza, A.M. Martinez, E.E. Silva, V.R. Melian, O.J. Venturini, O.A.d. Olmo, Optimization of a Dish Stirling system working with DIR-type receiver using multi-objective techniques, 204 (2017) 271-286.
[23] F.A. Boyaghchi, H. Molaie, Advanced exergy and environmental analyses and multi objective optimization of a real combined cycle power plant with supplementary firing using evolutionary algorithm, Energy, 93 (2015) 2267-2279.
[24] M. Mehrabi, S.M. Pesteei, T. Pashaee, Modeling of heat transfer and fluid flow characteristics of helicoidal double-pipe heat exchangers using Adaptive Neuro-Fuzzy Inference System (ANFIS), International Communications in Heat and Mass Transfer, 38 (2011) 525-532.
[25] S. Rezazadeh, M. Mehrabi, S.M. Pesteei, I. Mirzaee, Using adaptive neuro-fuzzy inference system (ANFIS) for proton exchange membrane fuel cell (PEMFC) performance modeling, Journal of Mechanical Science and Technology, 26 (2012) 3701-3709.
[26] H. Jalalifar, S. Mojedifar, A.A. Sahebi, H. Nezamabadi-pour, Application of the adaptive neuro-fuzzy inference system for prediction of a rock engineering classification system, Computers and Geotechnics, 38 (2011) 783-790.
[27] J.S.R. Jang, ANFIS: adaptive network-based fuzzy inference system, IEEE Transactions on Systems, Man, and Cybernetics, 23 (1993) 665-685.
[28] S. Chiu, Fuzzy Model Identification Based on Cluster Estimation, Journal of Intelligent & Fuzzy Systems, 2 (1994) 267-278.
[29] J.C. Dunn, A fuzzy relative of the ISODATA process and its use in detecting compact well-separated clusters, Journal of Cybernetics, 3 (1973) 32-57.
[30] J.C. Bezdek, Pattern recognition with fuzzy objective function algorithms, Plenum, New York, (1981).
[31] J.C. Bezdek, R. Ehrlich, W. Full, FCM: The fuzzy C-means clustering algorithm, Computers & Geosciences, 10 (1984) 191-203.
[32] C.W. Hirt, B.D. Nichols, Volume of fluid (VOF) method for the dynamics of free boundaries, Journal of Comptational Physics, 39 (1981) 201-225.
[33] Z. Yang, T.H. Shih, New time scale based k-ε model for near wall turbulence, AIAA Journal, 317 (1993) 1191-1197.
[34] Z. Liu, B. Sunden, J. Yuan, VOF Modeling and Analysis of Film wise Condensation Between Vertical Parallel Plates, Heat Transfer Research, 43 (2012) 47-68.
[35] W.H. Lee, A Pressure Iteration Scheme for Two-Phase Flow Modeling, Multiphase Transport: Fundamentals, Reactor Safety, Applications, Verizoglu, T. N., ed., Hemisphere Publishing, Washington, DC, (1980).
[36] B. Vadgama, D.K. Harris, Measurements of the contact angle between R134a and both aluminium and copper surfaces, Experimental Thermal and Fluid Sciences 31 (2007) 979-984.
[37] S.M.A.N.R. Abadi, J.P. Meyer, J. Dirker, Numerical investigation of condensation inside an inclined smooth tube, Proceeding of 13th International Conference on Heat Transfer, Fluid Mechanics and Thermodynamics, Portoroz, Slovenia, (2017) 576-572.
[38] J.P. Meyer, J. Dirker, A.O. Adelaja, Condensation heat transfer in smooth inclined tubes for R134a at different saturation temperatures, International Journal of Heat and Mass Transfer, 70 (2014) 515-525.
[39] A.O. Adelaja, J. Dirker, J.P. Meyer, Experimental study of the pressure drop during condensation in an inclined smooth tube at different saturation temperatures International Journal of Heat and Mass Transfer, 105 (2017) 237-251.

[40] S. Lips, J.P. Meyer, Two-phase flow in inclined tubes with specific reference to condensation: A review, International Journal of Multiphase Flow, 37 (2011) 845-859.
[41] S. Lips, J.P. Meyer, Experimental study of convective condensation of R134a in an inclined tube, Proceeding of 8th International Conference on Heat Transfer, Fluid Mechanics and Thermodynamics, Pointe Aux Piments, Mauritius, (2011) 38-43.
[42] S. Lips, J.P. Meyer, Experimental study of convective condensation in an inclined smooth tube. Part I: Inclination effect on flow pattern and heat transfer coefficient, International Journal of Heat and Mass Transfer, 55 (2012) 395-404.
[43] S. Lips, J.P. Meyer, Experimental study of convective condensation in an inclined smooth tube. Part II: Inclination effect on pressure drops and void fractions, International Journal of Heat and Mass Transfer, 55 (2012) 405-412.
[44] S. Lips, J.P. Meyer, Effect of Gravity Forces on Heat Transfer and Pressure DropDuring Condensation of R134a, Microgravity Science and Technology, 24 (2012) 157-164.

List of figure captions

Fig. 1. Schematic of the ANFIS architecture.

Fig. 2 Effect of grid size: (a) condensation heat transfer coefficient, and (b) pressure drop along tube.

Fig. 3. Schematic of the experiment setup [38].

Fig. 4. Comparison between the performances of the three proposed ANFIS models for the training of condensation heat transfer coefficient for T_{sat} = 40 °C and G = 100 kg/m²s, with (a) x_m = 0.25 and (b) x_m = 0.75.

Fig. 5. Comparison between the performances of the three proposed ANFIS models for the training of the pressure drop along the tube for T_{sat} = 30 °C and G = 100 kg/m²s, with (a) x_m = 0.25 and (b) x_m = 0.75.

Fig. 6. Comparison between the performances of the two proposed ANFIS models for the prediction of condensation heat transfer coefficient for (a) T_{sat} = 45 °C, G = 200 kg/m²s, and x_m = 0.5, (b) T_{sat} = 45 °C, G = 200 kg/m²s, and x_m = 0.5, (c) T_{sat} = 35 °C, G = 200 kg/m²s, and x_m = 0.5.

Fig. 7. Comparison between the performances of the two proposed ANFIS models for the prediction of the pressure drop along the tube for (a) T_{sat} = 40 °C, G = 400 kg/m²s, and x_m = 0.5 and (b) T_{sat} = 30 °C, G = 300 kg/m²s, and x_m = 0.25.

Fig. 8. Results of the ANFIS model and experiment data for predicting the condensation heat transfer coefficient at different tube inclination angles and mass fluxes for T_{sat} = 30 °C, with (a) x_m = 0.25, (b) x_m = 0.5, and (c) x_m = 0.75.

Fig. 9. Results of the ANFIS model and experiment data for predicting the pressure drop along the tube at different tube inclination angles and mass fluxes for T_{sat} = 30 °C, with (a) x_m = 0.25, (b) x_m = 0.5, and (c) x_m = 0.75.

Fig. 10. Comparison between the present numerical results and experiment data by Adelaja *et al.* [39] for the pressure drop along the tube for T_{sat} = 40 °C, G = 100 kg/m²s, and x_m = 0.5.

Fig. 11. Comparison between the present numerical results and experiment data by Meyer *et al.* [38] for the condensation heat transfer coefficient along the tube for T_{sat} = 35 °C, G = 200 kg/m²s, and x_m = 0.5.

Fig. 12. Comparison between the present numerical results and experiment data by Meyer *et al.* [38] for the condensation heat transfer coefficient along the tube for T_{sat} = 45 °C, G = 200 kg/m²s, and x_m = 0.5.

Fig. 13. Comparison between the present numerical results and experiment data of Adelaja *et al.* [39] for the pressure drop along the tube for T_{sat} = 40 °C, G = 400 kg/m²s, and x_m = 0.5.

Fig. 14. Comparison between the present numerical results and experiment data by Meyer *et al.* [38] for the condensation heat transfer coefficient for T_{sat} = 40 °C, G = 300 kg/m²s, and x_m = 0.25.

Fig. 15. Comparison between the present numerical results and experiment data by Meyer *et al.* [38] for the condensation heat transfer coefficient for T_{sat} = 40 °C, G = 100 kg/m²s, and x_m = 0. 5.

Fig. 16. Multi-objective Pareto front of the condensation heat transfer coefficient and pressure drop along the tube.

List of table captions

Table 1. Statistical criteria used for the analysis of the results.

Table 2. Results of training errors for the average condensation heat transfer coefficient of R134a model using different structure identification methods.

Table 3. Results of training errors for the pressure drop of R134a model using different structure identification methods.

Table 4. Parameters of ANFIS membership functions for modelling of the average condensation heat transfer coefficient (h_{ave}) and pressure drop (ΔP) of R134a within an inclined smooth tube.

Table 5. Fuzzy rule base and ANFIS output for modelling of the average condensation heat transfer coefficient of R134a within an inclined smooth tube.

Table 6. Fuzzy rule base and ANFIS output for modelling of the pressure drop of R134a within an inclined smooth tube.

Table 7. The range of variations for the parameters used in multi-objective optimization.

Figures:

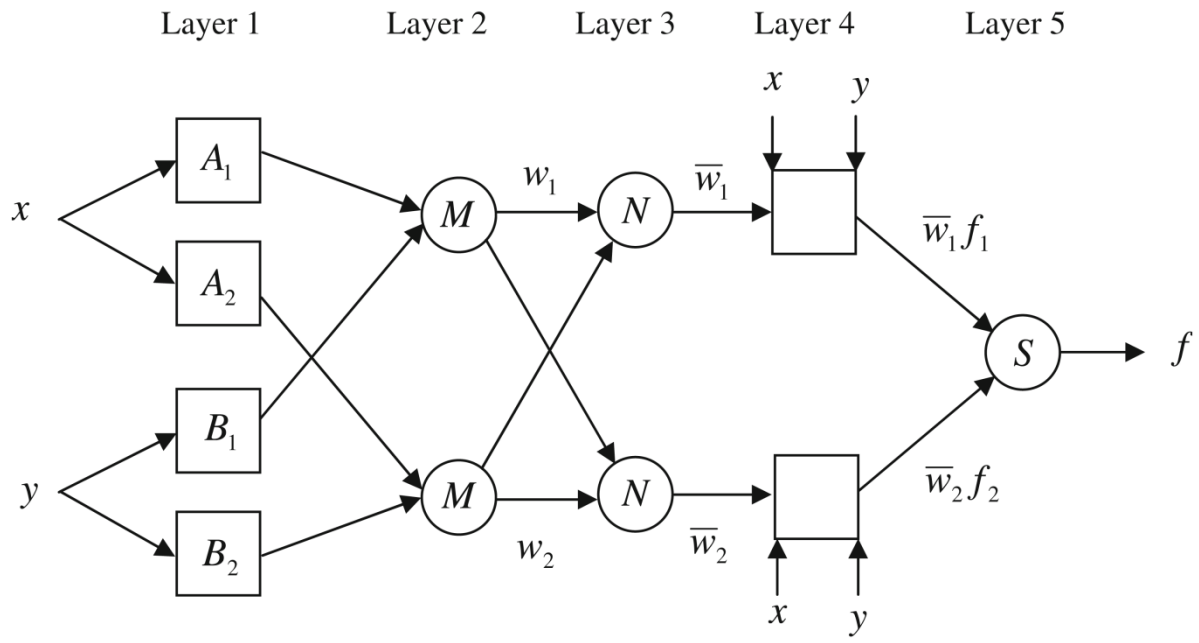

Fig. 1

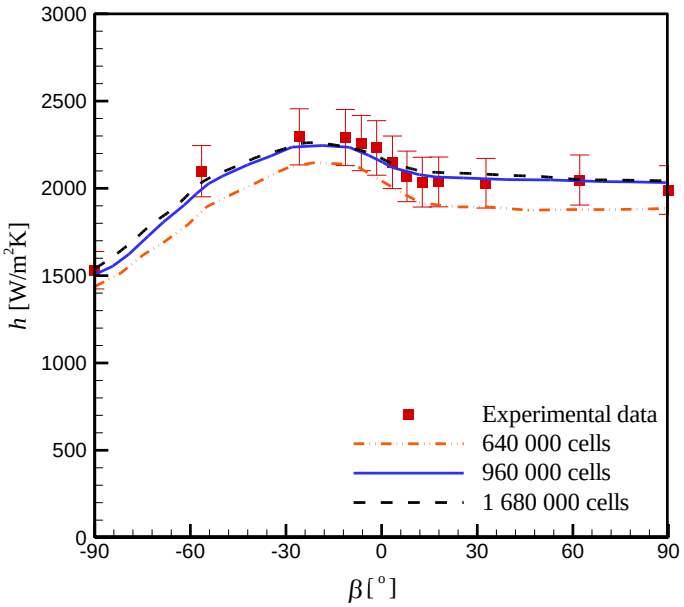
3000
2500
2000
1500
1000
500
0
h [W/m²K]
-90
-60
-30
0
30
60
90
β[°]
Experimental data
640 000 cells
960 000 cells
1 680 000 cells

(a)

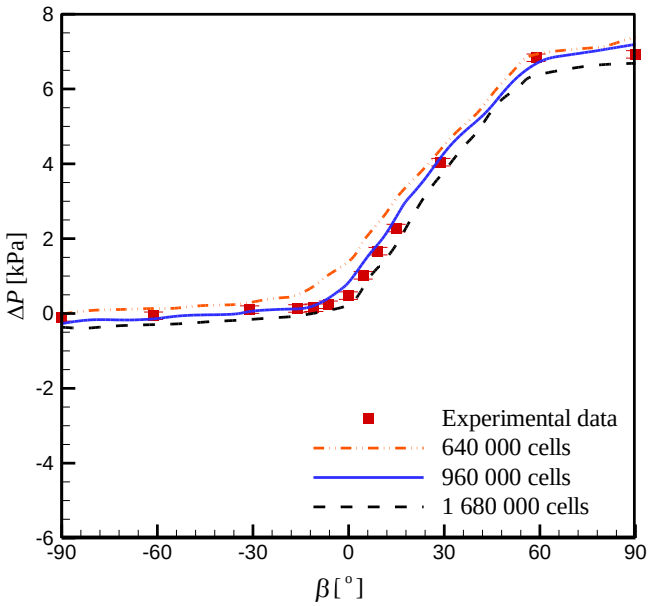
8
6
4
2
0
-2
-4
-6
ΔP [kPa]
-90
-60
-30
0
30
60
90
β[°]
Experimental data
640 000 cells
960 000 cells
1 680 000 cells

(b)

Fig. 2

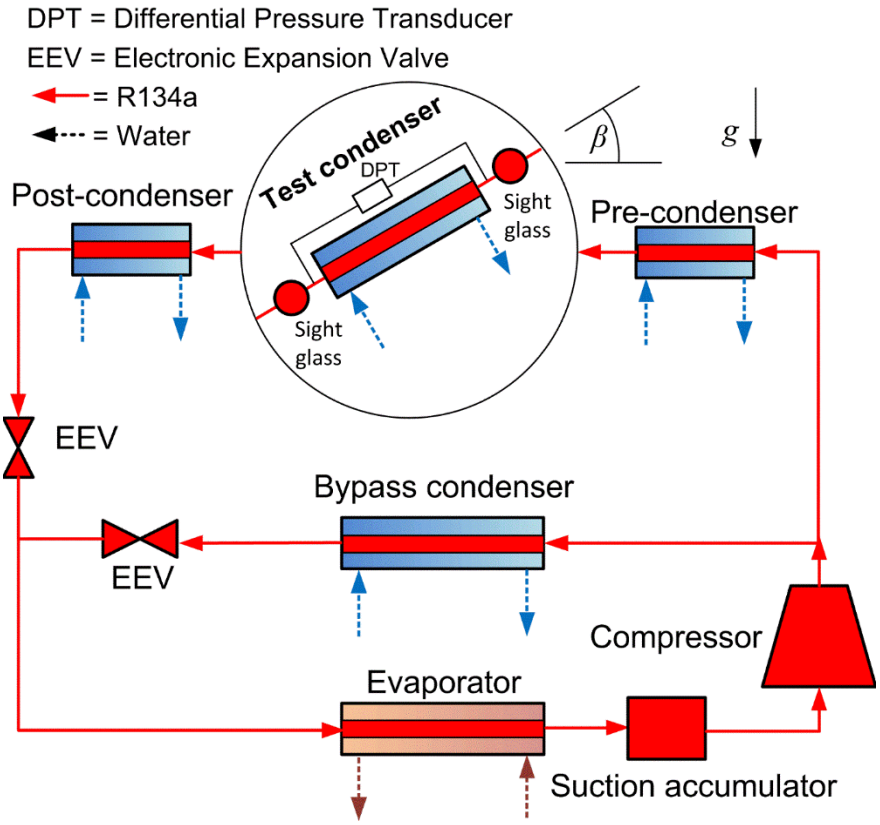
DPT = Differential Pressure Transducer
EEV = Electronic Expansion Valve
= R134a
= Water
Test condenser
DPT
Sight glass
Sight glass
β
g
Post-condenser
Pre-condenser
EEV
Bypass condenser
EEV
Compressor
Evaporator
Suction accumulator

Fig. 3

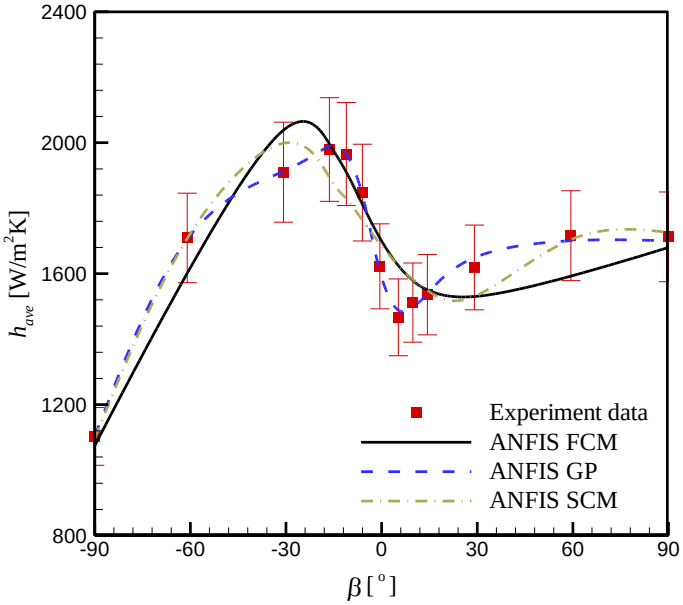
2400
2000
1600
1200
800
h_{ave} [W/m^{2}K]
-90
-60
-30
0
30
60
90
β [°]
Experiment data
ANFIS FCM
ANFIS GP
ANFIS SCM

(a)

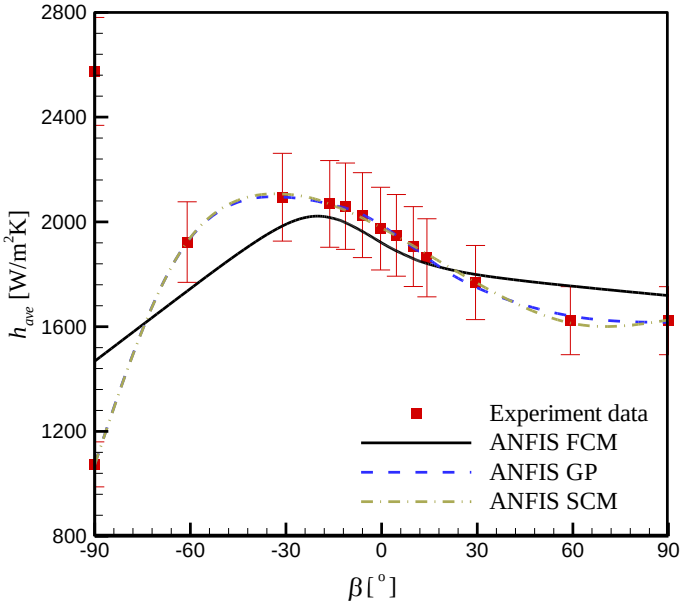
2800
2400
2000
1600
1200
800
h_{ave} [W/m^{2}K]
-90
-60
-30
0
30
60
90
β [°]
Experiment data
ANFIS FCM
ANFIS GP
ANFIS SCM

(b)

Fig. 4

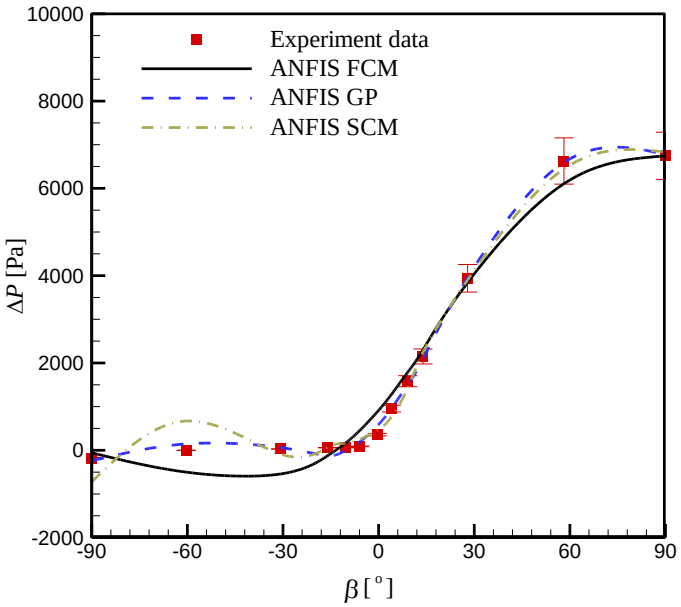
Experiment data
ANFIS FCM
ANFIS GP
ANFIS SCM
ΔP [Pa]
β [°]
10000
8000
6000
4000
2000
0
-2000
-90
-60
-30
0
30
60
90

(a)

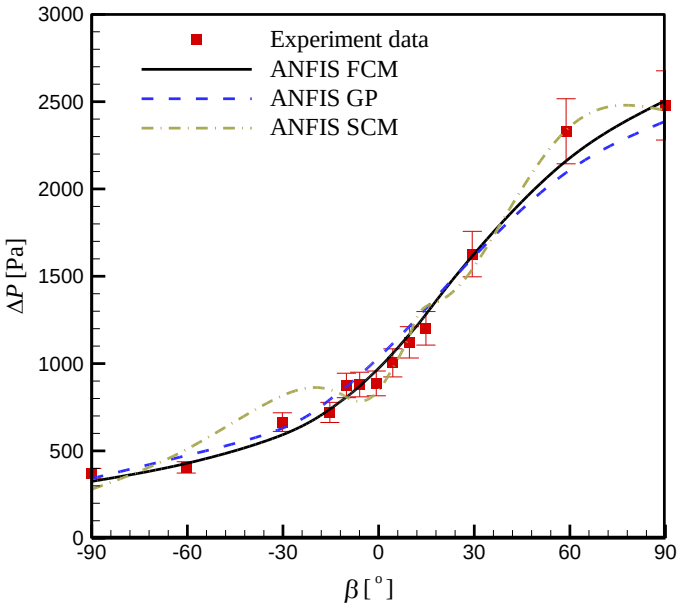
Experiment data
ANFIS FCM
ANFIS GP
ANFIS SCM
ΔP [Pa]
β [°]
3000
2500
2000
1500
1000
500
0
-90
-60
-30
0
30
60
90

(b)

Fig. 5

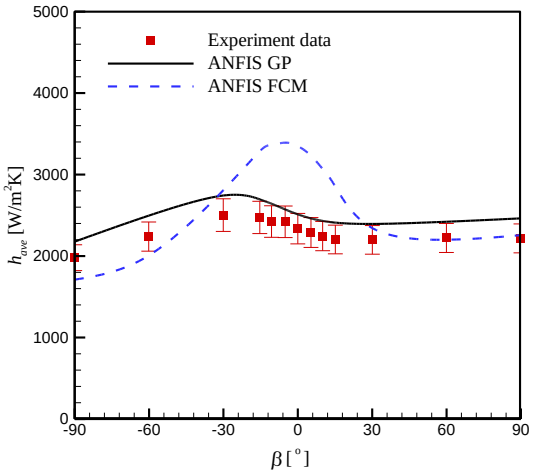
Experiment data
ANFIS GP
ANFIS FCM
h_{ave} [W/m^{2}K]
β[°]

(a)

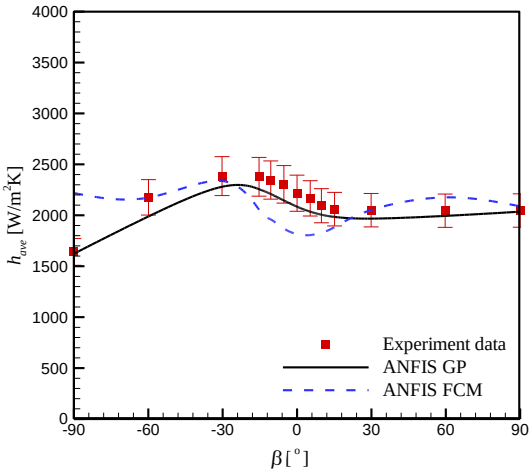
Experiment data
ANFIS GP
ANFIS FCM
h_{ave} [W/m^{2}K]
β[°]

(b)

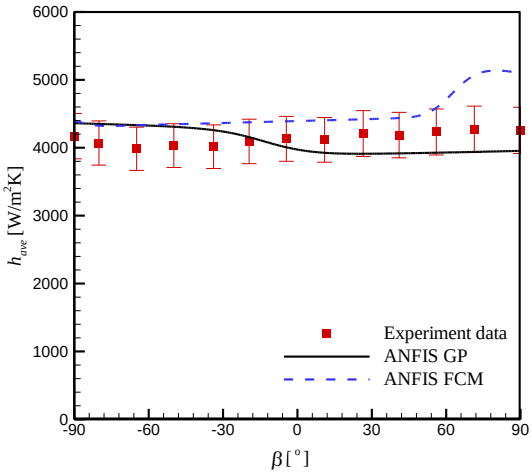
Experiment data
ANFIS GP
ANFIS FCM
h_{ave} [W/m^{2}K]
β[°]

(c)

Fig. 6

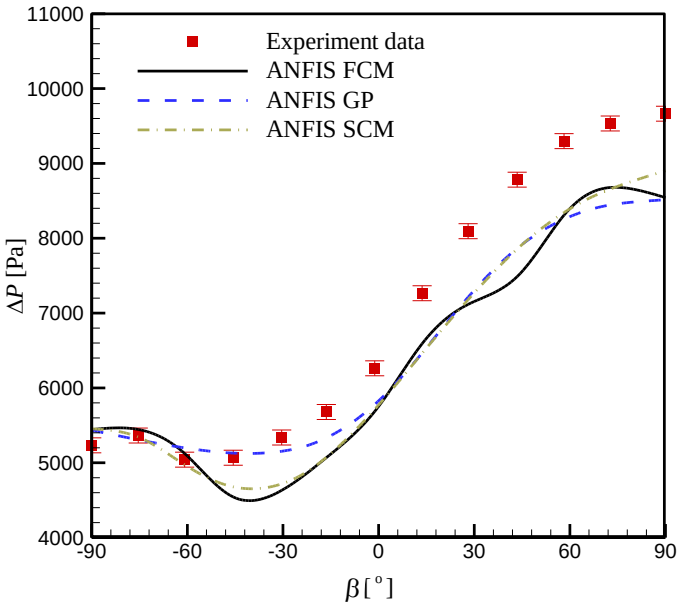
Experiment data
ANFIS FCM
ANFIS GP
ANFIS SCM
ΔP [Pa]
β [°]
11000
10000
9000
8000
7000
6000
5000
4000
-90
-60
-30
0
30
60
90

(a)

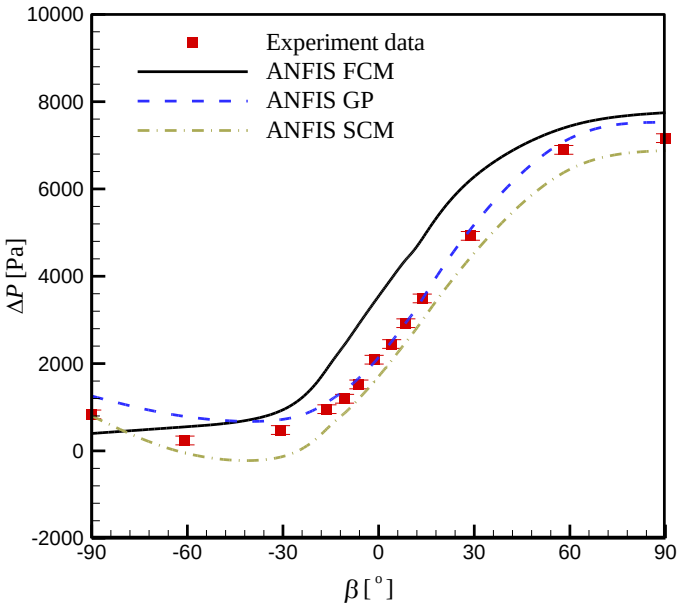
Experiment data
ANFIS FCM
ANFIS GP
ANFIS SCM
ΔP [Pa]
β [°]
10000
8000
6000
4000
2000
0
-2000
-90
-60
-30
0
30
60
90

(b)

Fig. 7

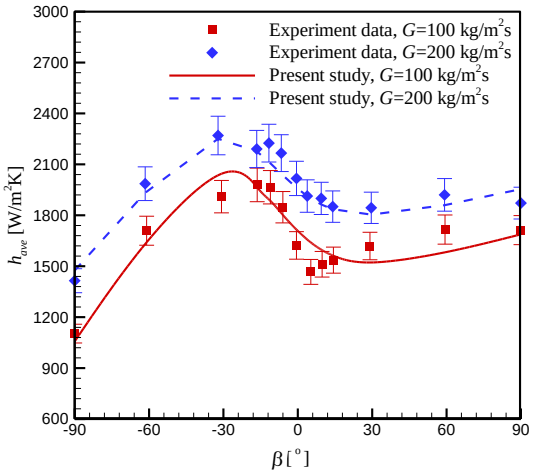
Experiment data, G=100 kg/m2s
Experiment data, G=200 kg/m2s
Present study, G=100 kg/m2s
Present study, G=200 kg/m2s
h_ave [W/m2K]
β[°]

(a)

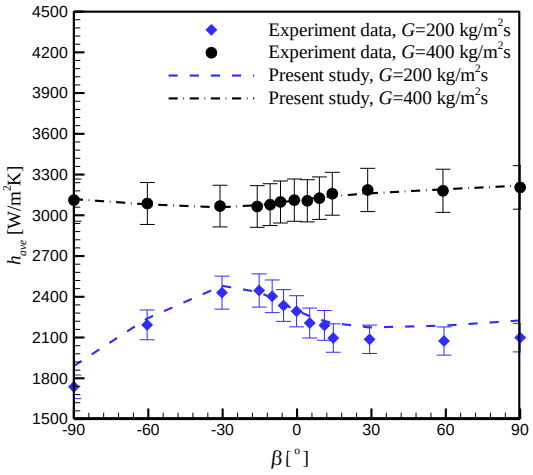
Experiment data, G=200 kg/m2s
Experiment data, G=400 kg/m2s
Present study, G=200 kg/m2s
Present study, G=400 kg/m2s
h_ave [W/m2K]
β[°]

(b)

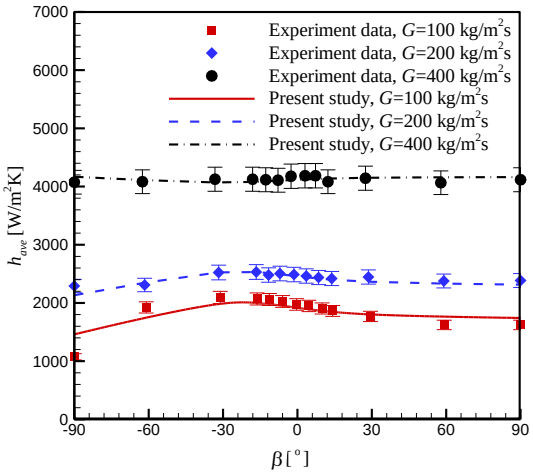
Experiment data, G=100 kg/m2s
Experiment data, G=200 kg/m2s
Experiment data, G=400 kg/m2s
Present study, G=100 kg/m2s
Present study, G=200 kg/m2s
Present study, G=400 kg/m2s
h_ave [W/m2K]
β[°]

(c)

Fig. 8

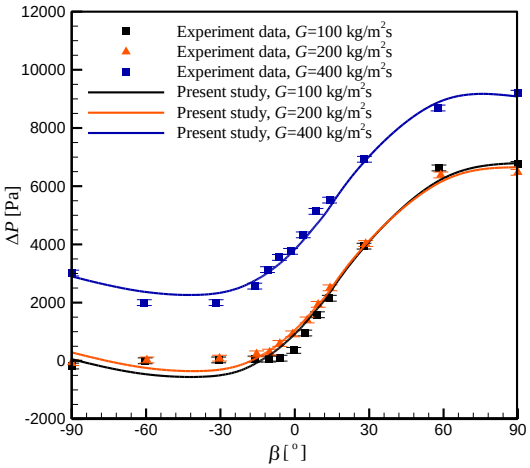
Experiment data, G=100 kg/m2s
Experiment data, G=200 kg/m2s
Experiment data, G=400 kg/m2s
Present study, G=100 kg/m2s
Present study, G=200 kg/m2s
Present study, G=400 kg/m2s
ΔP [Pa]
β [°]

(a)

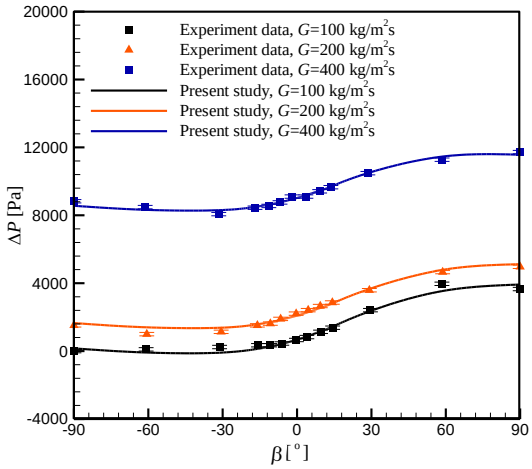
Experiment data, G=100 kg/m2s
Experiment data, G=200 kg/m2s
Experiment data, G=400 kg/m2s
Present study, G=100 kg/m2s
Present study, G=200 kg/m2s
Present study, G=400 kg/m2s
ΔP [Pa]
β [°]

(b)

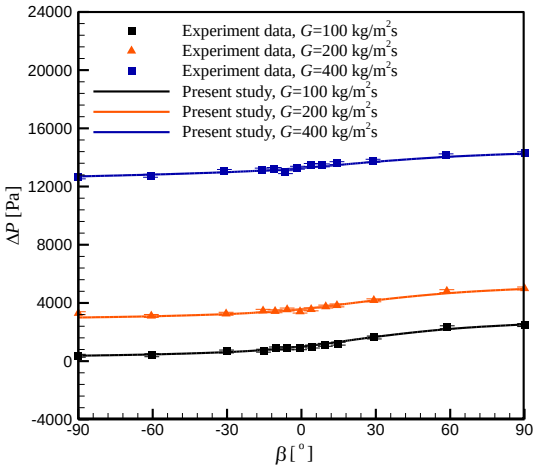
Experiment data, G=100 kg/m2s
Experiment data, G=200 kg/m2s
Experiment data, G=400 kg/m2s
Present study, G=100 kg/m2s
Present study, G=200 kg/m2s
Present study, G=400 kg/m2s
ΔP [Pa]
β [°]

(c)

Fig. 9

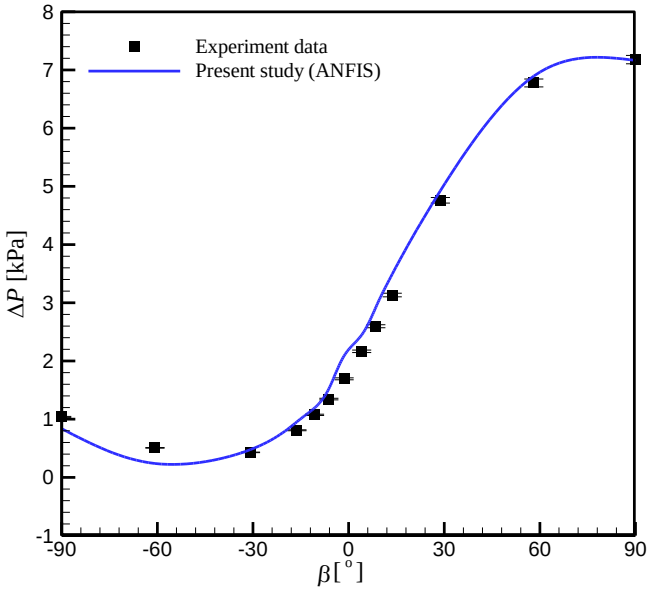
Experiment data
Present study (ANFIS)
ΔP [kPa]
β[°]
8
7
6
5
4
3
2
1
0
-1
-90
-60
-30
0
30
60
90

Fig. 10

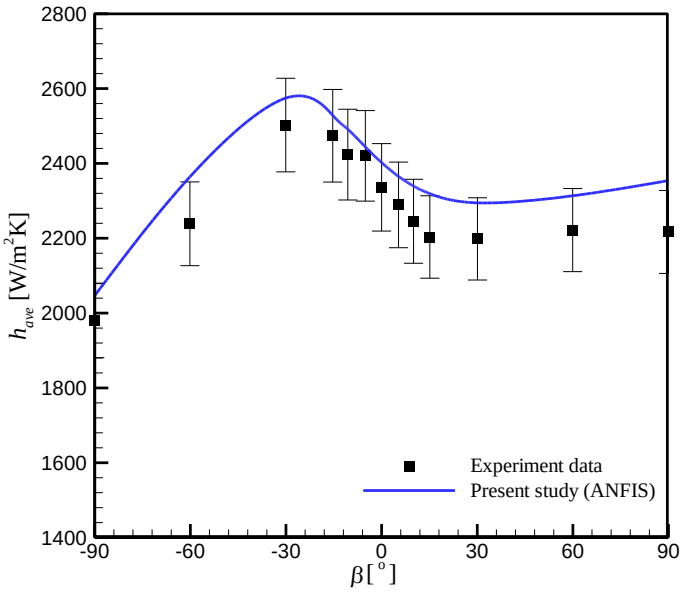
2800
2600
2400
2200
2000
1800
1600
1400
h_{ave} [W/m^{2}K]
-90
-60
-30
0
30
60
90
β[^{o}]
Experiment data
Present study (ANFIS)

Fig. 11

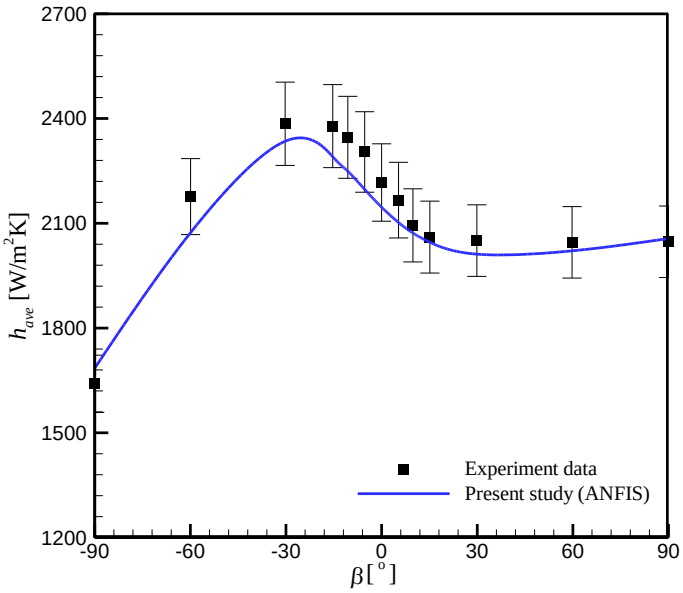
2700
2400
2100
1800
1500
1200
h_{ave} [W/m^{2}K]
-90
-60
-30
0
30
60
90
β[^{o}]
Experiment data
Present study (ANFIS)

Fig. 12

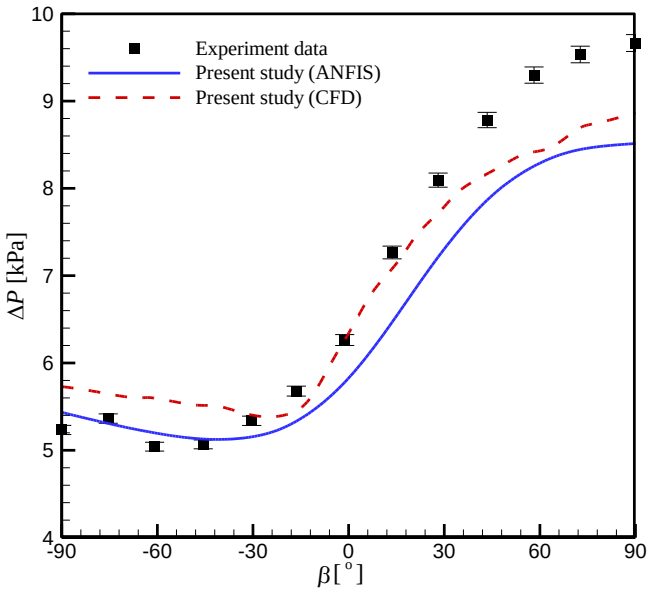
Experiment data
Present study (ANFIS)
Present study (CFD)
ΔP [kPa]
β[°]
10
9
8
7
6
5
4
-90
-60
-30
0
30
60
90

Fig. 13

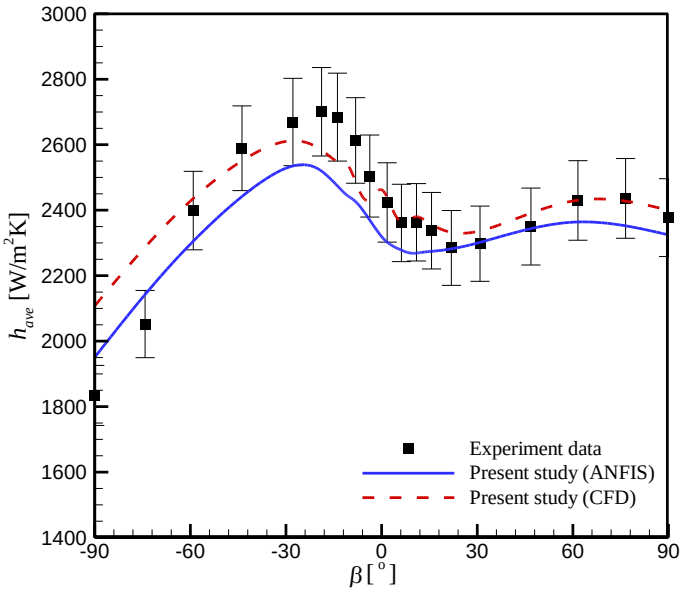
3000
2800
2600
2400
2200
2000
1800
1600
1400
h_{ave} [W/m^{2}K]
-90
-60
-30
0
30
60
90
β[^{o}]
Experiment data
Present study (ANFIS)
Present study (CFD)

Fig. 14

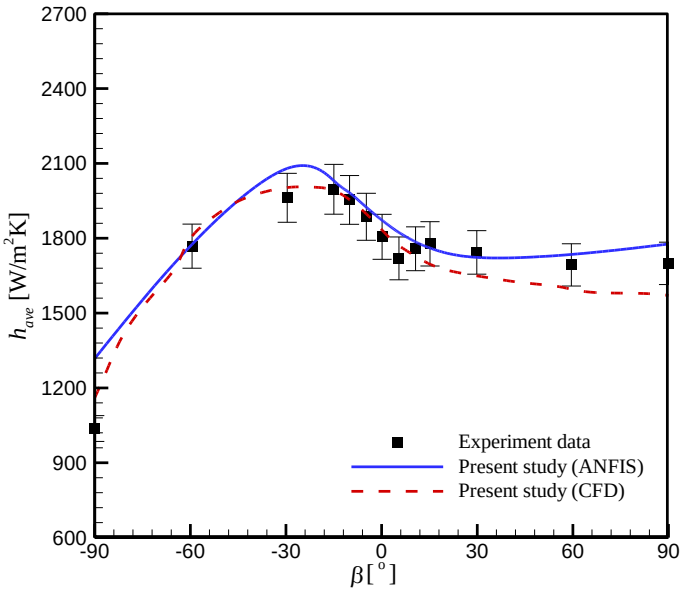
2700
2400
2100
1800
1500
1200
900
600
h_{ave} [W/m^{2}K]
-90
-60
-30
0
30
60
90
β[^{o}]
Experiment data
Present study (ANFIS)
Present study (CFD)

Fig. 15

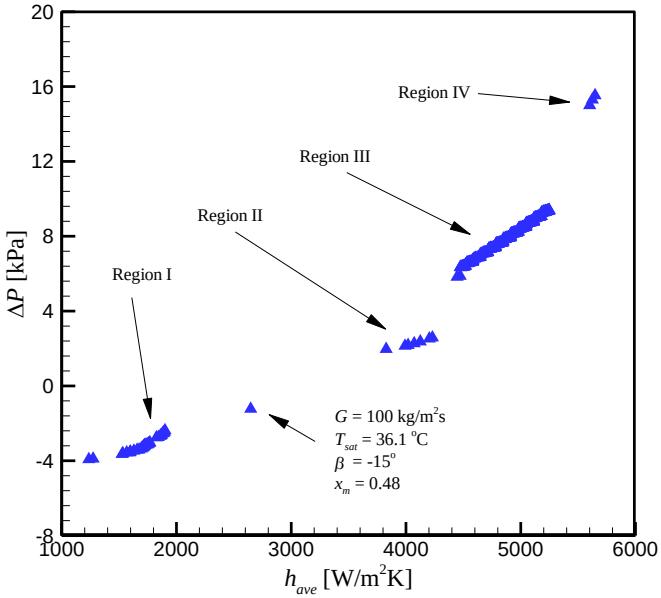
20
16
12
8
4
0
-4
-8
ΔP [kPa]
1000
2000
3000
4000
5000
6000
h_ave [W/m²K]
Region IV
Region III
Region II
Region I
G = 100 kg/m²s
T_sat = 36.1 °C
β = -15°
x_m = 0.48

Fig. 16

Tables:

Table 1. Statistical criteria used for the analysis of the results

Statistical criterion	Equation
Mean absolute error	$MAE = \frac{1}{n}\sum_{i=1}^{n}\left\|X_p - X_a\right\|$
Mean relative error	$MRE(\%) = \frac{100}{n}\sum_{i=1}^{n}\left(\frac{\left\|X_p - X_a\right\|}{X_a}\right)$
Root mean square error	$RMSE = \sqrt{\frac{1}{n}\sum_{i=1}^{n}\left(X_p - X_a\right)^2}$

$\boldsymbol{X_p}$ is the predicted value and $\boldsymbol{X_a}$ is the actual (experiment) data

Table 2. Results of training errors for the average condensation heat transfer coefficient of R134a model using different structure identification methods

	MAE	*MRE*	*RMSE*
Grid partitioning (GP)	47.19	2.33%	66.74
subtractive clustering method (SCM)	76.75	3.85%	102.86
fuzzy C-means (FCM) clustering	57.89	2.87%	73.03

Table 3. Results of training errors for the pressure drop of R134a model using different structure identification methods

	MAE	*MRE*	*RMSE*
Grid partitioning (GP)	75.37	6.38%	96.63
Subtractive clustering method (SCM)	115.52	9.15%	173.59
Fuzzy C-means (FCM) clustering	107.97	6.91%	146.33

Table 4. Parameters of ANFIS membership functions for modelling of the average condensation heat transfer coefficient (h_{ave}) and pressure drop (ΔP) of R134a within an inclined smooth tube

Membership function	Input 1 $\boldsymbol{G}$ (kg/m^2.s)			Input 2 $\boldsymbol{T_{sat}}$ (^{o}C)			Input 3 $\boldsymbol{x_m}$			Input 4 $\boldsymbol{\beta}$ (Radian)		
	a	***b***	***c***	***a***	***b***	***c***	***a***	***b***	***c***	***a***	***b***	***c***
h_{ave}												
MF1	150	1.451	99.98	9.646	1.704	29.61	0.2775	2.001	0.2827	1.116	2.258	-1.759
MF2	150	1.93	400	10.36	2.329	49.59	0.2376	1.998	0.7766	0.9718	2.547	1.103
Δp												
MF1	250	2.145	99.99	9.232	1.075	29.15	0.2592	2.013	0.3522	1.406	1.887	-1.504
MF2	250	2.274	600	10.83	2.866	48.99	0.3184	1.981	0.8032	1.481	1.558	2.266

a, ***b***, *and* ***c*** represent generalised bell-shaped membership function constants

Table 5. Fuzzy rule base and ANFIS output for modelling of the average condensation heat transfer coefficient of R134a within an inclined smooth tube

Number of Rules	Rule description
1	If ($\boldsymbol{G}$ is $\boldsymbol{G}$ MF1) and ($\boldsymbol{T_{sat}}$ is $\boldsymbol{T_{sat}}$ MF1) and ($\boldsymbol{x_m}$ is $\boldsymbol{x_m}$ MF1) and ($\boldsymbol{\beta}$ is $\boldsymbol{\beta}$ MF1) then $\boldsymbol{h_{ave}} = a_{1,1} \times \boldsymbol{G} + a_{1,2} \times \boldsymbol{T_{sat}} + a_{1,3} \times \boldsymbol{x_m} + a_{1,4} \times \boldsymbol{\beta} + a_{1,5}$
2	If ($\boldsymbol{G}$ is $\boldsymbol{G}$ MF1) and ($\boldsymbol{T_{sat}}$ is $\boldsymbol{T_{sat}}$ MF1) and ($\boldsymbol{x_m}$ is $\boldsymbol{x_m}$ MF1) and ($\boldsymbol{\beta}$ is $\boldsymbol{\beta}$ MF2) then $\boldsymbol{h_{ave}} = a_{2,1} \times \boldsymbol{G} + a_{2,2} \times \boldsymbol{T_{sat}} + a_{2,3} \times \boldsymbol{x_m} + a_{2,4} \times \boldsymbol{\beta} + a_{2,5}$
3	If ($\boldsymbol{G}$ is $\boldsymbol{G}$ MF1) and ($\boldsymbol{T_{sat}}$ is $\boldsymbol{T_{sat}}$ MF1) and ($\boldsymbol{x_m}$ is $\boldsymbol{x_m}$ MF2) and ($\boldsymbol{\beta}$ is $\boldsymbol{\beta}$ MF1) then $\boldsymbol{h_{ave}} = a_{3,1} \times \boldsymbol{G} + a_{3,2} \times \boldsymbol{T_{sat}} + a_{3,3} \times \boldsymbol{x_m} + a_{3,4} \times \boldsymbol{\beta} + a_{3,5}$
4	If ($\boldsymbol{G}$ is $\boldsymbol{G}$ MF1) and ($\boldsymbol{T_{sat}}$ is $\boldsymbol{T_{sat}}$ MF1) and ($\boldsymbol{x_m}$ is $\boldsymbol{x_m}$ MF2) and ($\boldsymbol{\beta}$ is $\boldsymbol{\beta}$ MF2) then $\boldsymbol{h_{ave}} = a_{4,1} \times \boldsymbol{G} + a_{4,2} \times \boldsymbol{T_{sat}} + a_{4,3} \times \boldsymbol{x_m} + a_{4,4} \times \boldsymbol{\beta} + a_{4,5}$
5	If ($\boldsymbol{G}$ is $\boldsymbol{G}$ MF1) and ($\boldsymbol{T_{sat}}$ is $\boldsymbol{T_{sat}}$ MF2) and ($\boldsymbol{x_m}$ is $\boldsymbol{x_m}$ MF1) and ($\boldsymbol{\beta}$ is $\boldsymbol{\beta}$ MF1) then $\boldsymbol{h_{ave}} = a_{5,1} \times \boldsymbol{G} + a_{5,2} \times \boldsymbol{T_{sat}} + a_{5,3} \times \boldsymbol{x_m} + a_{5,4} \times \boldsymbol{\beta} + a_{5,5}$
6	If ($\boldsymbol{G}$ is $\boldsymbol{G}$ MF1) and ($\boldsymbol{T_{sat}}$ is $\boldsymbol{T_{sat}}$ MF2) and ($\boldsymbol{x_m}$ is $\boldsymbol{x_m}$ MF1) and ($\boldsymbol{\beta}$ is $\boldsymbol{\beta}$ MF2) then $\boldsymbol{h_{ave}} = a_{6,1} \times \boldsymbol{G} + a_{6,2} \times \boldsymbol{T_{sat}} + a_{6,3} \times \boldsymbol{x_m} + a_{6,4} \times \boldsymbol{\beta} + a_{6,5}$
7	If ($\boldsymbol{G}$ is $\boldsymbol{G}$ MF1) and ($\boldsymbol{T_{sat}}$ is $\boldsymbol{T_{sat}}$ MF2) and ($\boldsymbol{x_m}$ is $\boldsymbol{x_m}$ MF2) and ($\boldsymbol{\beta}$ is $\boldsymbol{\beta}$ MF1) then $\boldsymbol{h_{ave}} = a_{7,1} \times \boldsymbol{G} + a_{7,2} \times \boldsymbol{T_{sat}} + a_{7,3} \times \boldsymbol{x_m} + a_{7,4} \times \boldsymbol{\beta} + a_{7,5}$
8	If ($\boldsymbol{G}$ is $\boldsymbol{G}$ MF1) and ($\boldsymbol{T_{sat}}$ is $\boldsymbol{T_{sat}}$ MF2) and ($\boldsymbol{x_m}$ is $\boldsymbol{x_m}$ MF2) and ($\boldsymbol{\beta}$ is $\boldsymbol{\beta}$ MF2) then $\boldsymbol{h_{ave}} = a_{8,1} \times \boldsymbol{G} + a_{8,2} \times \boldsymbol{T_{sat}} + a_{8,3} \times \boldsymbol{x_m} + a_{8,4} \times \boldsymbol{\beta} + a_{8,5}$
9	If ($\boldsymbol{G}$ is $\boldsymbol{G}$ MF2) and ($\boldsymbol{T_{sat}}$ is $\boldsymbol{T_{sat}}$ MF1) and ($\boldsymbol{x_m}$ is $\boldsymbol{x_m}$ MF1) and ($\boldsymbol{\beta}$ is $\boldsymbol{\beta}$ MF1) then $\boldsymbol{h_{ave}} = a_{9,1} \times \boldsymbol{G} + a_{9,2} \times \boldsymbol{T_{sat}} + a_{9,3} \times \boldsymbol{x_m} + a_{9,4} \times \boldsymbol{\beta} + a_{9,5}$
10	If ($\boldsymbol{G}$ is $\boldsymbol{G}$ MF2) and ($\boldsymbol{T_{sat}}$ is $\boldsymbol{T_{sat}}$ MF1) and ($\boldsymbol{x_m}$ is $\boldsymbol{x_m}$ MF1) and ($\boldsymbol{\beta}$ is $\boldsymbol{\beta}$ MF2) then $\boldsymbol{h_{ave}} = a_{10,1} \times \boldsymbol{G} + a_{10,2} \times \boldsymbol{T_{sat}} + a_{10,3} \times \boldsymbol{x_m} + a_{10,4} \times \boldsymbol{\beta} + a_{10,5}$
11	If ($\boldsymbol{G}$ is $\boldsymbol{G}$ MF2) and ($\boldsymbol{T_{sat}}$ is $\boldsymbol{T_{sat}}$ MF1) and ($\boldsymbol{x_m}$ is $\boldsymbol{x_m}$ MF2) and ($\boldsymbol{\beta}$ is $\boldsymbol{\beta}$ MF1) then $\boldsymbol{h_{ave}} = a_{11,1} \times \boldsymbol{G} + a_{11,2} \times \boldsymbol{T_{sat}} + a_{11,3} \times \boldsymbol{x_m} + a_{11,4} \times \boldsymbol{\beta} + a_{11,5}$
12	If ($\boldsymbol{G}$ is $\boldsymbol{G}$ MF2) and ($\boldsymbol{T_{sat}}$ is $\boldsymbol{T_{sat}}$ MF1) and ($\boldsymbol{x_m}$ is $\boldsymbol{x_m}$ MF2) and ($\boldsymbol{\beta}$ is $\boldsymbol{\beta}$ MF2) then $\boldsymbol{h_{ave}} = a_{12,1} \times \boldsymbol{G} + a_{12,2} \times \boldsymbol{T_{sat}} + a_{12,3} \times \boldsymbol{x_m} + a_{12,4} \times \boldsymbol{\beta} + a_{12,5}$
13	If ($\boldsymbol{G}$ is $\boldsymbol{G}$ MF2) and ($\boldsymbol{T_{sat}}$ is $\boldsymbol{T_{sat}}$ MF2) and ($\boldsymbol{x_m}$ is $\boldsymbol{x_m}$ MF1) and ($\boldsymbol{\beta}$ is $\boldsymbol{\beta}$ MF1) then $\boldsymbol{h_{ave}} = a_{13,1} \times \boldsymbol{G} + a_{13,2} \times \boldsymbol{T_{sat}} + a_{13,3} \times \boldsymbol{x_m} + a_{13,4} \times \boldsymbol{\beta} + a_{13,5}$
14	If ($\boldsymbol{G}$ is $\boldsymbol{G}$ MF2) and ($\boldsymbol{T_{sat}}$ is $\boldsymbol{T_{sat}}$ MF2) and ($\boldsymbol{x_m}$ is $\boldsymbol{x_m}$ MF1) and ($\boldsymbol{\beta}$ is $\boldsymbol{\beta}$ MF2) then $\boldsymbol{h_{ave}} = a_{14,1} \times \boldsymbol{G} + a_{14,2} \times \boldsymbol{T_{sat}} + a_{14,3} \times \boldsymbol{x_m} + a_{14,4} \times \boldsymbol{\beta} + a_{14,5}$
15	If ($\boldsymbol{G}$ is $\boldsymbol{G}$ MF2) and ($\boldsymbol{T_{sat}}$ is $\boldsymbol{T_{sat}}$ MF2) and ($\boldsymbol{x_m}$ is $\boldsymbol{x_m}$ MF2) and ($\boldsymbol{\beta}$ is $\boldsymbol{\beta}$ MF1) then $\boldsymbol{h_{ave}} = a_{15,1} \times \boldsymbol{G} + a_{15,2} \times \boldsymbol{T_{sat}} + a_{15,3} \times \boldsymbol{x_m} + a_{15,4} \times \boldsymbol{\beta} + a_{15,5}$
16	If ($\boldsymbol{G}$ is $\boldsymbol{G}$ MF2) and ($\boldsymbol{T_{sat}}$ is $\boldsymbol{T_{sat}}$ MF2) and ($\boldsymbol{x_m}$ is $\boldsymbol{x_m}$ MF2) and ($\boldsymbol{\beta}$ is $\boldsymbol{\beta}$ MF2) then $\boldsymbol{h_{ave}} = a_{16,1} \times \boldsymbol{G} + a_{16,2} \times \boldsymbol{T_{sat}} + a_{16,3} \times \boldsymbol{x_m} + a_{16,4} \times \boldsymbol{\beta} + a_{16,5}$

Table 6. Fuzzy rule base and ANFIS output for modelling of the pressure drop of R134a within an inclined smooth tube

Number of Rules	Rule description
1	If ($\boldsymbol{G}$ is $\boldsymbol{G}$ MF1) and ($\boldsymbol{T_{sat}}$ is $\boldsymbol{T_{sat}}$ MF1) and ($\boldsymbol{x_m}$ is $\boldsymbol{x_m}$ MF1) and ($\boldsymbol{\beta}$ is $\boldsymbol{\beta}$ MF1) then $\Delta P = b_{1,1}\times \boldsymbol{G} + b_{1,2}\times \boldsymbol{T_{sat}} + b_{1,3}\times \boldsymbol{x_m} + b_{1,4}\times \boldsymbol{x_m} + b_{1,5}$
2	If ($\boldsymbol{G}$ is $\boldsymbol{G}$ MF1) and ($\boldsymbol{T_{sat}}$ is $\boldsymbol{T_{sat}}$ MF1) and ($\boldsymbol{x_m}$ is $\boldsymbol{x_m}$ MF1) and ($\boldsymbol{\beta}$ is $\boldsymbol{\beta}$ MF2) then $\Delta P = b_{2,1}\times \boldsymbol{G} + b_{2,2}\times \boldsymbol{T_{sat}} + b_{2,3}\times \boldsymbol{x_m} + b_{2,4}\times \boldsymbol{x_m} + b_{2,5}$
3	If ($\boldsymbol{G}$ is $\boldsymbol{G}$ MF1) and ($\boldsymbol{T_{sat}}$ is $\boldsymbol{T_{sat}}$ MF1) and ($\boldsymbol{x_m}$ is $\boldsymbol{x_m}$ MF2) and ($\boldsymbol{\beta}$ is $\boldsymbol{\beta}$ MF1) then $\Delta P = b_{3,1}\times \boldsymbol{G} + b_{3,2}\times \boldsymbol{T_{sat}} + b_{3,3}\times \boldsymbol{x_m} + b_{3,4}\times \boldsymbol{x_m} + b_{3,5}$
4	If ($\boldsymbol{G}$ is $\boldsymbol{G}$ MF1) and ($\boldsymbol{T_{sat}}$ is $\boldsymbol{T_{sat}}$ MF1) and ($\boldsymbol{x_m}$ is $\boldsymbol{x_m}$ MF2) and ($\boldsymbol{\beta}$ is $\boldsymbol{\beta}$ MF2) then $\Delta P = b_{4,1}\times \boldsymbol{G} + b_{4,2}\times \boldsymbol{T_{sat}} + b_{4,3}\times \boldsymbol{x_m} + b_{4,4}\times \boldsymbol{x_m} + b_{4,5}$
5	If ($\boldsymbol{G}$ is $\boldsymbol{G}$ MF1) and ($\boldsymbol{T_{sat}}$ is $\boldsymbol{T_{sat}}$ MF2) and ($\boldsymbol{x_m}$ is $\boldsymbol{x_m}$ MF1) and ($\boldsymbol{\beta}$ is $\boldsymbol{\beta}$ MF1) then $\Delta P = b_{5,1}\times \boldsymbol{G} + b_{5,2}\times \boldsymbol{T_{sat}} + b_{5,3}\times \boldsymbol{x_m} + b_{5,4}\times \boldsymbol{x_m} + b_{5,5}$
6	If ($\boldsymbol{G}$ is $\boldsymbol{G}$ MF1) and ($\boldsymbol{T_{sat}}$ is $\boldsymbol{T_{sat}}$ MF2) and ($\boldsymbol{x_m}$ is $\boldsymbol{x_m}$ MF1) and ($\boldsymbol{\beta}$ is $\boldsymbol{\beta}$ MF2) then $\Delta P = b_{6,1}\times \boldsymbol{G} + b_{6,2}\times \boldsymbol{T_{sat}} + b_{6,3}\times \boldsymbol{x_m} + b_{6,4}\times \boldsymbol{x_m} + b_{6,5}$
7	If ($\boldsymbol{G}$ is $\boldsymbol{G}$ MF1) and ($\boldsymbol{T_{sat}}$ is $\boldsymbol{T_{sat}}$ MF2) and ($\boldsymbol{x_m}$ is $\boldsymbol{x_m}$ MF2) and ($\boldsymbol{\beta}$ is $\boldsymbol{\beta}$ MF1) then $\Delta P = b_{7,1}\times \boldsymbol{G} + b_{7,2}\times \boldsymbol{T_{sat}} + b_{7,3}\times \boldsymbol{x_m} + b_{7,4}\times \boldsymbol{x_m} + b_{7,5}$
8	If ($\boldsymbol{G}$ is $\boldsymbol{G}$ MF1) and ($\boldsymbol{T_{sat}}$ is $\boldsymbol{T_{sat}}$ MF2) and ($\boldsymbol{x_m}$ is $\boldsymbol{x_m}$ MF2) and ($\boldsymbol{\beta}$ is $\boldsymbol{\beta}$ MF2) then $\Delta P = b_{8,1}\times \boldsymbol{G} + b_{8,2}\times \boldsymbol{T_{sat}} + b_{8,3}\times \boldsymbol{x_m} + b_{8,4}\times \boldsymbol{x_m} + b_{8,5}$
9	If ($\boldsymbol{G}$ is $\boldsymbol{G}$ MF2) and ($\boldsymbol{T_{sat}}$ is $\boldsymbol{T_{sat}}$ MF1) and ($\boldsymbol{x_m}$ is $\boldsymbol{x_m}$ MF1) and ($\boldsymbol{\beta}$ is $\boldsymbol{\beta}$ MF1) then $\Delta P = b_{9,1}\times \boldsymbol{G} + b_{9,2}\times \boldsymbol{T_{sat}} + b_{9,3}\times \boldsymbol{x_m} + b_{9,4}\times \boldsymbol{x_m} + b_{9,5}$
10	If ($\boldsymbol{G}$ is $\boldsymbol{G}$ MF2) and ($\boldsymbol{T_{sat}}$ is $\boldsymbol{T_{sat}}$ MF1) and ($\boldsymbol{x_m}$ is $\boldsymbol{x_m}$ MF1) and ($\boldsymbol{\beta}$ is $\boldsymbol{\beta}$ MF2) then $\Delta P = b_{10,1}\times \boldsymbol{G} + b_{10,2}\times \boldsymbol{T_{sat}} + b_{10,3}\times \boldsymbol{x_m} + b_{10,4}\times \boldsymbol{x_m} + b_{10,5}$
11	If ($\boldsymbol{G}$ is $\boldsymbol{G}$ MF2) and ($\boldsymbol{T_{sat}}$ is $\boldsymbol{T_{sat}}$ MF1) and ($\boldsymbol{x_m}$ is $\boldsymbol{x_m}$ MF2) and ($\boldsymbol{\beta}$ is $\boldsymbol{\beta}$ MF1) then $\Delta P = b_{11,1}\times \boldsymbol{G} + b_{11,2}\times \boldsymbol{T_{sat}} + b_{11,3}\times \boldsymbol{x_m} + b_{11,4}\times \boldsymbol{x_m} + b_{11,5}$
12	If ($\boldsymbol{G}$ is $\boldsymbol{G}$ MF2) and ($\boldsymbol{T_{sat}}$ is $\boldsymbol{T_{sat}}$ MF1) and ($\boldsymbol{x_m}$ is $\boldsymbol{x_m}$ MF2) and ($\boldsymbol{\beta}$ is $\boldsymbol{\beta}$ MF2) then $\Delta P = b_{12,1}\times \boldsymbol{G} + b_{12,2}\times \boldsymbol{T_{sat}} + b_{12,3}\times \boldsymbol{x_m} + b_{12,4}\times \boldsymbol{x_m} + b_{12,5}$
13	If ($\boldsymbol{G}$ is $\boldsymbol{G}$ MF2) and ($\boldsymbol{T_{sat}}$ is $\boldsymbol{T_{sat}}$ MF2) and ($\boldsymbol{x_m}$ is $\boldsymbol{x_m}$ MF1) and ($\boldsymbol{\beta}$ is $\boldsymbol{\beta}$ MF1) then $\Delta P = b_{13,1}\times \boldsymbol{G} + b_{13,2}\times \boldsymbol{T_{sat}} + b_{13,3}\times \boldsymbol{x_m} + b_{13,4}\times \boldsymbol{x_m} + b_{13,5}$
14	If ($\boldsymbol{G}$ is $\boldsymbol{G}$ MF2) and ($\boldsymbol{T_{sat}}$ is $\boldsymbol{T_{sat}}$ MF2) and ($\boldsymbol{x_m}$ is $\boldsymbol{x_m}$ MF1) and ($\boldsymbol{\beta}$ is $\boldsymbol{\beta}$ MF2) then $\Delta P = b_{14,1}\times \boldsymbol{G} + b_{14,2}\times \boldsymbol{T_{sat}} + b_{14,3}\times \boldsymbol{x_m} + b_{14,4}\times \boldsymbol{x_m} + b_{14,5}$
15	If ($\boldsymbol{G}$ is $\boldsymbol{G}$ MF2) and ($\boldsymbol{T_{sat}}$ is $\boldsymbol{T_{sat}}$ MF2) and ($\boldsymbol{x_m}$ is $\boldsymbol{x_m}$ MF2) and ($\boldsymbol{\beta}$ is $\boldsymbol{\beta}$ MF1) then $\Delta P = b_{15,1}\times \boldsymbol{G} + b_{15,2}\times \boldsymbol{T_{sat}} + b_{15,3}\times \boldsymbol{x_m} + b_{15,4}\times \boldsymbol{x_m} + b_{15,5}$
16	If ($\boldsymbol{G}$ is $\boldsymbol{G}$ MF2) and ($\boldsymbol{T_{sat}}$ is $\boldsymbol{T_{sat}}$ MF2) and ($\boldsymbol{x_m}$ is $\boldsymbol{x_m}$ MF2) and ($\boldsymbol{\beta}$ is $\boldsymbol{\beta}$ MF2) then $\Delta P = b_{16,1}\times \boldsymbol{G} + b_{16,2}\times \boldsymbol{T_{sat}} + b_{16,3}\times \boldsymbol{x_m} + b_{16,4}\times \boldsymbol{x_m} + b_{16,5}$

Table 7. The range of variations for the parameters used in multi-objective optimization.

Parameter	Range
G [kg/m^{2}s]	100 - 500
x_m [-]	0.1 - 0.9
T_{sat} [°C]	30 - 50
β [°]	-90 - 90

Appendix

$$[\mathbf{a}_{i,j}] = \begin{bmatrix} 1.775 & 101.3 & 1001 & 1456 & 1.534 \\ 2.852 & 28.7 & 675.1 & 211.7 & 0.5333 \\ 2.75 & 83.77 & -453.5 & 132 & 1.293 \\ 1.816 & 76.39 & -305.7 & 11.29 & 1.132 \\ 5.004 & 21.76 & 1108 & 940.5 & 2.089 \\ 0.4373 & 16.47 & 1379 & 212 & 0.7029 \\ 10.62 & 21.96 & -501.8 & 790.5 & 1.782 \\ 7.755 & 14.19 & -625.4 & -165.7 & 1.554 \\ 8.141 & -22.43 & 324.8 & -729.3 & 0.0752 \\ 2.349 & 72.98 & 219.8 & -72.88 & 1.207 \\ 11.62 & -23.15 & -147.8 & -605.8 & -0.373 \\ 6.552 & 52.79 & -99.11 & -30.32 & 0.7967 \\ 0.4197 & 41.92 & 359.6 & 240.9 & 0.07014 \\ 0.8228 & 26.21 & 448.7 & 160.3 & 1.618 \\ 12.38 & -7.636 & -163.8 & 137.1 & -0.509 \\ 9.956 & 10.82 & -202.8 & 37.43 & 1.081 \end{bmatrix}$$

$$[\mathbf{b}_{i,j}] = \begin{bmatrix} -3.494 & -195.4 & 1459 & -1629 & 2550 \\ -10.24 & 211.1 & -7379 & -726.4 & 5784 \\ 23.74 & -132.5 & 681 & 365.2 & 1543 \\ 21.06 & -321.8 & 6782 & 588.5 & 3487 \\ 10.95 & 11.94 & 2940 & 973.6 & -4545 \\ 46.58 & 226.2 & -2734 & 144.9 & -10270 \\ 39.05 & -33.12 & -3935 & 479.3 & -2752 \\ 69.6 & 50.64 & -4287 & -614.3 & -6218 \\ -15.16 & -208.9 & 22070 & -1832 & 5973 \\ -25.74 & 292.5 & 11490 & -2228 & 13530 \\ 11.77 & 486.4 & -7546 & 711.7 & 3637 \\ 11.31 & 86.04 & 1770 & 682.3 & 8186 \\ 29.98 & -97.52 & 1980 & -1637 & -10630 \\ 71.79 & 6.479 & -11780 & -151.7 & -24030 \\ 54.29 & -133.5 & -6802 & -497.4 & -6439 \\ 74.9 & -169.3 & -7392 & -36.74 & -14550 \end{bmatrix}$$